SANDIA REPORT

SAND87 — 1977 • UC — 70
Unlimited Release
Printed October 1987

A Constitutive Model for the Consolidation of WIPP Crushed Salt and Its Use in Analyses of Backfilled Shaft and Drift Configurations

G. D. Sjaardema, R. D. Krieg

Prepared by
Sandia National Laboratories
Albuquerque, New Mexico 87185 and Livermore, California 94550
for the United States Department of Energy
under Contract DE-AC04-76DP00789

SF2900Q(8-81)

Issued by Sandia National Laboratories, operated for the United States Department of Energy by Sandia Corporation.

Printed in the United States of America
Available from
National Technical Information Service
U.S. Department of Commerce
5285 Port Royal Road
Springfield, VA 22161

NTIS price codes
Printed copy: A04
Microfiche copy: A01

SAND87-1977
Unlimited Release
Printed October 1987

Distribution
UC-70

A Constitutive Model for the Consolidation of WIPP Crushed Salt and Its Use in Analyses of Backfilled Shaft and Drift Configurations

G. D. Sjaardema and R. D. Krieg
Applied Mechanics Division I
Sandia National Laboratories
Albuquerque, New Mexico 87185

Abstract

A constitutive model for the consolidation of wet crushed salt material is presented in this report. The material parameters for this model are derived from hydrostatic consolidation tests performed on wet salt taken from the Waste Isolation Pilot Plant (WIPP) near Carlsbad, New Mexico. The constitutive model is then used for analyses of the interaction between intact and crushed salt in realistic field configurations such as backfilled and open shafts and drifts. The calculations are used to show that the wet crushed salt does not significantly retard the rate of closure of shafts and drifts until the crushed salt is consolidated to approximately 95 percent of intact salt density. An approximate method for modeling the creep rate of intact salt is developed which more closely matches the closure data from empty drifts at the WIPP site in order to provide a more realistic estimate of the crushed salt response.

Contents

Figures 6

Tables 8

1 Introduction 9

1.1 Testing of Crushed Salt Material 9

1.2 Organization 10

2 Data Reduction Procedure 11

2.1 Basic Definitions and Nomenclature 11

2.2 Experimental Work 12

2.3 Data Reduction Procedure 12

2.4 Pressure Dependence of Consolidation Rate 13

2.5 Density Dependence of Consolidation Rate 14

2.6 Remarks 15

3 Constitutive Equation for Crushed Salt 23

3.1 Previous Constitutive Models 23

3.2 Basic Definitions and Assumptions 24

3.3 Volumetric Constitutive Model 24

3.3.1 Integration of the Volumetric Constitutive Equation . . . 25

3.4 Deviatoric Constitutive Model 28

3.4.1 Elastic Deviatoric Model 28

3.4.2 Elastic–Plastic Deviatoric Model 29

3.4.3 Elastic–Creeping Model 30

3.5 Summary of the Constitutive Model 30

4 Analyses using the Crushed Salt Constitutive Model 33
4.1 Single Element Analyses 33
4.2 Shaft Analyses 33
4.2.1 Accelerated Creep of Intact Salt 34
4.2.2 Baseline Shaft Analysis 35
4.2.3 Backfilled Shaft Analyses 35
4.3 Drift Analyses 37
5 Summary and Conclusions 53
References 55
A Functional Form of the Elastic Moduli 59
B User's Instructions for SANCHO 61
C Determination of Crushed Salt Yield Strength 63

Figures

2.1 Pressure History for Test 240C61 18

2.2 Consolidation Rate vs. Density for Hydrostatic Consolidation Tests on Wet Crushed Salt 19

2.3 Fractional Density vs. Time for Test 23JL51 19

2.4 Consolidation Rate (Shifted for Pressure) vs. Density for Hydrostatic Consolidation Tests on Wet Crushed Salt 20

2.5 Comparison of Measured and Predicted Volumetric Creep for Confining Pressure = 1.72 MPa 20

2.6 Comparison of Measured and Predicted Volumetric Creep for Confining Pressure = 3.44 MPa 21

2.7 Comparison of Measured and Predicted Volumetric Creep for Confining Pressure = 0.69 MPa 21

2.8 Comparison of Measured and Predicted Volumetric Creep for Variable Pressure Test 240C61 22

4.1 Shaft Configuration 39

4.2 Comparison of Closure Rates for Reference and Reduced Moduli Shaft Analyses 40

4.3 Comparison of Closure for Reference and Reduced Moduli Shaft Analyses 40

4.4 Normalized Closure History for Baseline Shaft 41

4.5 Logarithmic Normalized Closure History for Baseline Shaft . . . 41

4.6 Logarithmic Normalized Closure Rate for Baseline Shaft 42

4.7 Normalized Shaft Closure for Deviatoric Behavior Analyses . . . 42

4.8 Fractional Density vs. Time for Emplacement Density Analyses . . 43

4.9 Density Ratio vs. Time for Emplacement Density Analyses . . . 43

4.10 Time Rate of Change of Density Ratio for Emplacement Density Analyses 44

4.11 Finite Element Mesh for the Crushed Salt, Intact Salt Interaction Analyses—Unbackfilled Drift 45

4.12 Close-up of the Drift Region Mesh for Crushed Salt, Intact Salt Interaction Analyses—Unbackfilled Drift 45

4.13 Deformed Shape of Square Corner Unbackfilled Drift at 20 Years . 46

4.14 Deformed Shape of Square Corner Unbackfilled Drift at 50 Years . 46

4.15 Closure Histories for Square Corner Unbackfilled Drift 47

4.16 Close-up of the Drift Region Mesh for Crushed Salt, Intact Salt Interaction Analyses—Backfilled Drift 47

4.17 Deformed Shape of Square Corner Backfilled Drift at 10 Years . . 48

4.18 Deformed Shape of Square Corner Backfilled Drift at 20 Years . . 48

4.19 Comparison of Closure Histories for Backfilled and Unbackfilled Drift 49

4.20 Density Contours for Square Corner Backfilled Drift at 10 Years . 49

4.21 Density Contours for Square Corner Backfilled Drift at 20 Years . 50

4.22 Close-up of the Drift Region for the Rounded Corner Drift . . . 50

4.23 Deformed Shape of Rounded Corner Open Drift at 20 Years . . . 51

4.24 Deformed Shape of Rounded Corner Open Drift at 49 Years . . . 51

A.1 Bulk Modulus Data for Dry Crushed Salt Material 60

C.1 Variation of Calculated Yield Stress with Fractional Density . . . 64

Tables

2.1 Results of Hydrostatic Consolidation Tests on WIPP Salt With Added Water [4] 17

2.2 Calculated Constants for Equation (2.3.2) * 18

4.1 Consolidation Times for Backfilled Shaft Analyses 39

A.1 Bulk Modulus Data for Dry Crushed Salt Material [8] 60

1. Introduction

The consolidation behavior of crushed, or granulated, salt is of interest to the Waste Isolation Pilot Plant (WIPP) project because salt removed from the excavations in the relatively pure rock salt is a likely material to be used as a backfill material and as a component of a multiple material sealing system. Crushed salt is expected to be an effective long term seal material because it readily consolidates to a dense state when subjected to sufficient confining pressure and because it is compatible with the host formation. It would be used around nuclear waste canisters, and then later as a void filler in storage rooms, shafts, and other openings when the facility is completed.

Rock salt has been used as backfill in mining operations in the past, particularly in potash mines. In that case, the crushed salt's primary function was to lessen subsidence seen at the ground level. For the WIPP it must also retard the migration of radionuclides and its performance in this regard must be predictable. Structural analyses are necessary to predict the long term response of storage drifts and the resulting compaction of the sealing and backfill material. These analyses require that a constitutive model describing the mechanical response of the crushed salt material be available.

At this time the type and composition of sealing materials for the WIPP has not been definitely decided because tests of the various candidate materials are still underway. However, the major sealing material will probably be crushed salt with a small amount of added water. Other candidate materials include mixtures of salt and bentonite, bentonite and sand, and bricks composed of compacted wet crushed salt or crushed salt and bentonite. This study was undertaken to determine the sensitivity of drift and shaft closure to the consolidation properties of the selected sealing material.

1.1 Testing of Crushed Salt Material

Laboratory testing of crushed salt has been performed by several investigators. The initial tests were performed with dry crushed salt. Hansen [3] performed a series of quasi-static and consolidation tests on granulated commercial-grade salt and Gnirk [2] performed consolidation tests on granulated salt from the Avery Island Mine. Holcomb and Hannum [8] performed several quasi-static and creep tests on salt from the Mississippi Chemical mine (south-east New Mexico) and from the

WIPP. These tests were done at temperatures of 20°, 40°, 60°, 80°, and 100° C, and hydrostatic stresses from 1.7 MPa to 21 MPa.

Recently Holcomb [5] showed that the addition of a small amount of water, less than approximately 2.5% by weight, to the crushed salt material significantly increases the consolidation rate relative to dry crushed salt material. Holcomb and Shields [4], and Pfeifle and Senseny [14] have since performed several tests on the wet crushed salt material. The results of Holcomb and Shields are of particular interest here because the tests were conducted on wet crushed salt material for long enough times and with a complete enough test matrix to characterize the volumetric creep behavior reasonably well. These test results have been used almost exclusively in this report.

1.2 Organization

This report presents a computational model for wet crushed salt including the derivation and integration of the constitutive model, the determination of the material parameters, and the results of several calculations performed using this model. Although models will have to be developed for each of the backfill materials selected for the WIPP and this entire process repeated each time, the procedures developed here for wet crushed salt should aid in the selection process. Preliminary experimental results have also shown that the consolidation behavior of the crushed salt and bentonite material is similar to the behavior of wet crushed salt [17]. If this trend is verified, the wet crushed salt constitutive model can be used to model the consolidation of the crushed salt and bentonite material simply with a change of material parameters.

The remainder of this report is organized as follows. The first section describes the experimental data upon which the model is based and the data fitting procedure used to determine the material constants. The next section is a derivation of the constitutive equation and describes how it is integrated. The results of several calculations performed with this model are then described. It then finishes with a summary of the report and a discussion of the direction of future work with the model.

2. Data Reduction Procedure

This section documents the data reduction method used to determine the parameters for the constitutive model describing the volumetric consolidation behavior of *wet* crushed salt material. The data used to determine these parameters are the results of the hydrostatic consolidation tests on WIPP salt with added water by Holcomb and Shields [4].

Wet crushed salt refers to crushed salt with a small amount of water added to increase the consolidation rate. The moisture content used in the tests varied from 0.5% to 3.0% water by weight. The minimum moisture content necessary to cause an increased consolidation rate has not yet been determined, but the increased consolidation rate has been seen for crushed salt with a moisture content of less than 0.5% by weight.

2.1 Basic Definitions and Nomenclature

The meanings of the symbols used in this chapter are:

e_v = Volumetric strain, positive in compression (decreasing volume)
P = Pressure, positive in compression
ρ = Absolute density measured in g/cc
ρ_0 = Density of material when $e_v = 0$
ρ_∞ = Density of intact salt, 2.14 g/cc
D = Fractional density = ρ/ρ_∞

The following conversions are used between volume strains and densities:

$$e_v = 1 - \rho_0/\rho \qquad (2.1.1)$$

$$\dot{e}_v = \rho_0\dot{\rho}/\rho^2 \qquad (2.1.2)$$

$$\rho = \rho_0/(1 - e_v) \qquad (2.1.3)$$

$$\rho \approx \rho_0(1 + e_v) \quad \text{for small } e_v \qquad (2.1.4)$$

$$\dot{\rho} = \frac{\rho_0\dot{e}_v}{(1 - e_v)^2} = \dot{e}_v\rho^2/\rho_0 \qquad (2.1.5)$$

A superposed dot indicates the time rate of change of the quantity.

2.2 Experimental Work

Holcomb and Shields have performed several hydrostatic consolidation tests on WIPP salt with added water [4]. The samples were cylindrical specimens 10.4 cm in diameter by 14.6 cm long and encased in thin lead jackets. The samples were tested by applying a uniform pressure on the entire surface of the sample. The uniform pressure was applied for a short period of time and then removed to preconsolidate the samples. The pressure was then reapplied and held constant while the volumetric change was noted as a function of time. The test duration was typically 23 days. Tests were conducted at room temperature under hydrostatic pressures of 1.72 MPa (250 psi) and 3.44 MPa (500 psi), and a range of moisture contents from 0.5 percent to 3.0 percent water by weight. Two other tests have been completed since the data reduction procedure described below was documented. Test 27JU61 [6] was conducted at a hydrostatic pressure of 0.69 MPa (100 psi), and test 240C61 [7] was conducted with a confining pressure which varied from 0.35 MPa (50 psi) to 6.90 MPa (1000 psi) in 5 increments over the duration of the test as shown in Figure 2.1. These last two tests were not available when the model was developed and the data reduction procedure was carried out. Instead, these tests are used for verification of the model. The procedure described here will be reapplied to update the material parameters when the data from all of the tests become available.

The volume strain histories from each creep test were found to be fitted very well by an empirical equation of the form

$$e_v = a \log_{10} t + c \tag{2.2.1}$$

where t is the time in seconds, and a and c are constants which were fitted in a least square manner to the data for each test. The values of a and c for each of the tests are taken from Holcomb [4] and reproduced in Table 2.1.

2.3 Data Reduction Procedure

The relationship described by Equation (2.2.1) can be approximated by a differential equation of the form

$$\dot{\rho} = B(P)e^{A\rho} \tag{2.3.1}$$

where ρ is the density of the sample, $\dot{\rho}$ is the time rate of change of the density, $B(P)$ is a function of the applied pressure, and A is a parameter to be determined. The parameters are not necessarily constants and can be functions of pressure, water content, or some other quantity.

Equation (2.3.1) is preferable to Equation (2.2.1) for our purposes here because explicit references to time have been eliminated and because the consolidation rate is explicitly given as a function of the absolute quantity, density, rather than a quantity such as e_v which has an arbitrary zero state. To determine the constants A and B in Equation (2.3.1), the volume strains were calculated using Equation (2.2.1) at 100 times equally spaced over the duration of the test. These volume strains were then converted to densities using Equation (2.1.3). The volumetric strain rate at each time interval was calculated by differentiating Equation (2.2.1) with respect to time. Equation (2.1.5) was then used to determine the consolidation rate corresponding to this volumetric strain rate. A linear regression procedure was then used to determine the least squares linear fit of the equation

$$\ln \dot{\rho} = B' + A\rho \tag{2.3.2}$$

to the calculated data for each test where B' is equal to $\ln B(P)$. The coefficients of correlation for each of the regression analyses were greater than 0.999 indicating that Equation (2.3.2) and therefore Equation (2.3.1) is an accurate approximation to Equation (2.2.1). The computed values of A and B' for each test are given in Table 2.2. Figure 2.2 is a plot of $\ln \dot{\rho}$ vs. ρ for each of the tests. The dashed lines indicate tests conducted at a confining pressure of 1.72 MPa; the solid lines indicate tests conducted at a confining pressure of 3.44 MPa; and the dotted line is the test conducted at a confining pressure of 0.69 MPa. The basic form of Equation (2.3.1) will be generalized to include the effect of pressure before the constants are determined.

2.4 Pressure Dependence of Consolidation Rate

The data shown in Figure 2.2 indicate that, at a given density, the consolidation rate is generally faster for the increased pressure tests, although test 19DC44 (curve K), consolidated at a slower rate than any of the 1.72 MPa tests. Another indication that the consolidation rate increases with increasing pressure is the 23JL51 (curve B) test data. This test was conducted with a confining pressure of 1.72 MPa for approximately 1.4 million seconds. The confining pressure was then increased to 2.52 MPa for approximately 150,000 seconds and then reduced to the original pressure for the remainder of the test. The consolidation rate during the increased pressure phase of this test is faster than the consolidation rates, at approximately the same densities, during the lower pressure phases of the test. Figure 2.3 is a plot of the fractional density vs. time for this test.

The 23JL51 test data were used to determine the pressure dependence of the consolidation rate. These data were used rather than determining the pressure dependence from two distinct tests at different pressures. In this way, the pressure dependence is isolated from the effects of the inherent sample-to-sample variation.

The different consolidation rates before and after the pressure changes are assumed to be caused only by the pressure variation. Therefore, the consolidation rates are related by

$$\frac{\dot{\rho}_{1.72}}{f(P=1.72)} = \frac{\dot{\rho}_{2.52}}{f(P=2.52)} \tag{2.4.1}$$

where $f(P)$ is a pressure function. The form of the pressure function chosen to describe this behavior is

$$f(P) = \exp(B_1 P) - 1 \tag{2.4.2}$$

where P is the pressure, positive in compression, and B_1 is a constant to be determined from the data. This pressure dependence is the same as that found for dry crushed salt where data at four different pressures were available [18]. Since the wet salt consolidation tests were conducted at only two distinct pressures, the form of the pressure function is not completely defined by the wet salt data alone.

The consolidation rate prior to the pressure increase in test 23JL51 is estimated to be $\dot{\rho} = 4.1\times10^{-8}$ g/cc·s. During the increased pressure phase, the consolidation rate is estimated to be $\dot{\rho} = 9.2\times10^{-8}$ g/cc·s. Using Equations (2.4.1) and (2.4.2), the constant B_1 is determined such that

$$\frac{\exp(1.72B_1) - 1}{\exp(2.52B_1) - 1} = \frac{4.1\times10^{-8}}{9.2\times10^{-8}} = 0.4493 \tag{2.4.3}$$

Solution of this equation results in a value of $B_1 \approx 0.82$. The pressure dependence of the consolidation rate is therefore:

$$f(P) = \exp(0.82P) - 1 \tag{2.4.4}$$

2.5 Density Dependence of Consolidation Rate

The pressure effect can be removed from the test data by dividing the consolidation rate by the pressure function (Equation (2.4.4)). Figure 2.4 is a plot of $\ln(\dot{\rho}/f(P))$ vs. ρ for all of the test data. The data show some scatter, but a definite grouping of the tests can be observed; the slopes of these curves are about the same. The remaining constants in Equation (2.3.1) were determined from these *pressure-shifted* data. A linear regression was used to give a least squares fit of all of the pressure-shifted data to an equation that is only a function of density. The resulting equation is

$$\ln\left[\frac{\dot{\rho}}{\exp(B_1 P) - 1}\right] = B_0' + A\rho = 12.7 - 17.3\rho \tag{2.5.1}$$

where B_0' is equal to $B'/f(P)$. Using these results and Equation (2.4.4), the final form of the consolidation equation for wet crushed salt is

$$\dot{\rho} = 1.3\mathrm{E}5[\mathrm{e}^{0.82P} - 1]\mathrm{e}^{-17.3\rho} \tag{2.5.2}$$

This equation is the same as Equation (2.3.1)

$$\text{where: } \begin{aligned} B &= B_0\left[e^{B_1 P} - 1\right], \\ B_0 &= 1.3\times10^5, \text{ and} \\ B_1 &= 0.82 \end{aligned}$$

Figures 2.5 and 2.6 are comparisons of the densities predicted by Equation (2.5.2) to those found in the consolidation tests for 1.72 MPa and 3.44 MPa confining pressures, respectively. The model falls almost in the middle of the data for each test. The model was then used to predict the responses of the two later tests that were not used to determine the model parameters. The results are shown in Figures 2.7 and 2.8 for tests 27JU61 and 24OC61, respectively. Note that Equation (2.5.2) overpredicts the 27JU61 data at later times. This trend is also evident in the 24OC61 comparison, however the agreement is remarkably good considering that these data were not used in the determination of the material parameters for the model.

2.6 Remarks

- The consolidation equation does not account for the effect of temperature on the consolidation rate—all of the tests were conducted at the same temperature. The form and constants of Equation (2.5.2) will have to be modified when data at other temperatures become available.

- Tests conducted at lower pressures are needed. Backfilled shaft and drift calculations performed with the model indicate that the maximum pressure in the backfill material is less than 0.5 MPa during most of the consolidation process for backfilled shafts and drifts at the WIPP. The consolidation behavior at these low pressures must be extrapolated by the model from the behavior at the test pressures (1.72 MPa and 3.44 MPa).

- The material constants developed in this section should only be used for the *wet* crushed salt material. The results of the tests on wet crushed salt backfill material do not show a strong correlation between the consolidation rate and the moisture content. The only correlation that has been found is that a small amount of added water greatly accelerates the consolidation rate compared to the consolidation rate of dry salt. The minimum moisture content required to achieve this accelerated rate has not yet been determined.

- The data from a limited number of tests were used to develop the model; additional tests are planned. The current constants may be modified as more test data become available.

- The results of consolidation tests on dry crushed salt backfill materials are also fitted very well [8] to an equation of the form of Equation (2.2.1). Therefore, the procedure outlined in this memo can also be used to reduce the data for those tests.

- A *slow* consolidation equation can be developed to bound the results of consolidation analyses. The stiffest or slowest consolidation rate was observed in test 19DC44. If the pressure dependence and the density dependence (constants A and B_1) are assumed to remain constant, a new value can be determined for the constant B_0 in Equation (2.5.1) to approximate the slow consolidation of this test. The resulting equation is

$$\dot{\rho}_{\mathrm{stiff}} = 5.42 \times 10^4 \left[e^{0.82P} - 1 \right] e^{-17.3\rho} \tag{2.6.1}$$

Table 2.1. Results of Hydrostatic Consolidation Tests on WIPP Salt With Added Water [4]

Curve	Test-ID	P_C	H_2O	D_0	D_q	D_{fm}	D_{fd}	a	c
A	27JU61	0.69	.025	.67	.70	.82	.82	5.3×10^{-2}	–.18
B	23JL51	1.72	.005	.70	.74	.84	.85	5.2×10^{-2}	–.15
C	14NV51	1.72	.015	.69	.73	.87	.89	6.8×10^{-2}	–.22
D	16FE61	1.72	.020	.68	.71	.85	.87	6.2×10^{-2}	–.19
E	10MY51	1.72	.024	.66	.74	.85	.88	5.8×10^{-2}	–.12
F	20AU51	1.72	.030	.63	.71	.88	.86	6.0×10^{-2}	–.11
G	16JL51	3.44	.005	.65	.74	.89	.89	5.4×10^{-2}	–.06
H	18JU51	3.44	.010	.68	.77	.90	.95	5.8×10^{-2}	–.08
I	300C51	3.44	.015	.69	.77	.91	.91	5.4×10^{-2}	–.09
J	16JA61	3.44	.020	.70	.76	.90	.91	5.3×10^{-2}	–.10
K	19DC44	3.44	.024	.66	.72	.87	.89	5.8×10^{-2}	–.14
L	13AU51	3.44	.030	.64	.74	.91	.89	5.2×10^{-2}	–.05

P_C is the hydrostatic pressure in MPa.
H_2O is the water content expressed as fraction of salt mass.
D_0 is the initial fractional sample density.
D_q is the fractional density after initial pressurization.
D_{fm} is the fractional density after the test as determined from immersion.
D_{fd} is the fractional density after the test as determined from the real time dilatometer readings.
All densities were computed using just the mass of the salt.
The test duration was typically 2,000,000 seconds.
Curve cross-references the Test-ID to the Figures.

Table 2.2. Calculated Constants for Equation (2.3.2)*

Curve	Test-ID	P_C	H_2O	ρ_0	A	B'
A	27JU61	0.69	.025	1.43	-22.3	20.2
B	23JL51	1.72	.005	1.50	-20.7	20.1
C	14NV51	1.72	.015	1.48	-14.9	10.6
D	16FE61	1.72	.020	1.46	-17.1	13.8
E	10MY51	1.72	.024	1.41	-16.6	13.8
F	20AU51	1.72	.030	1.35	-15.9	12.0
G	16JL51	3.44	.005	1.39	-16.5	14.6
H	18JU51	3.44	.010	1.46	-14.5	12.4
I	300C51	3.44	.015	1.48	-17.1	16.2
J	16JA61	3.44	.020	1.50	-18.1	17.8
K	19DC44	3.44	.024	1.41	-17.5	14.6
L	13AU51	3.44	.030	1.37	-17.5	15.8

*See Notes for Table 2.1

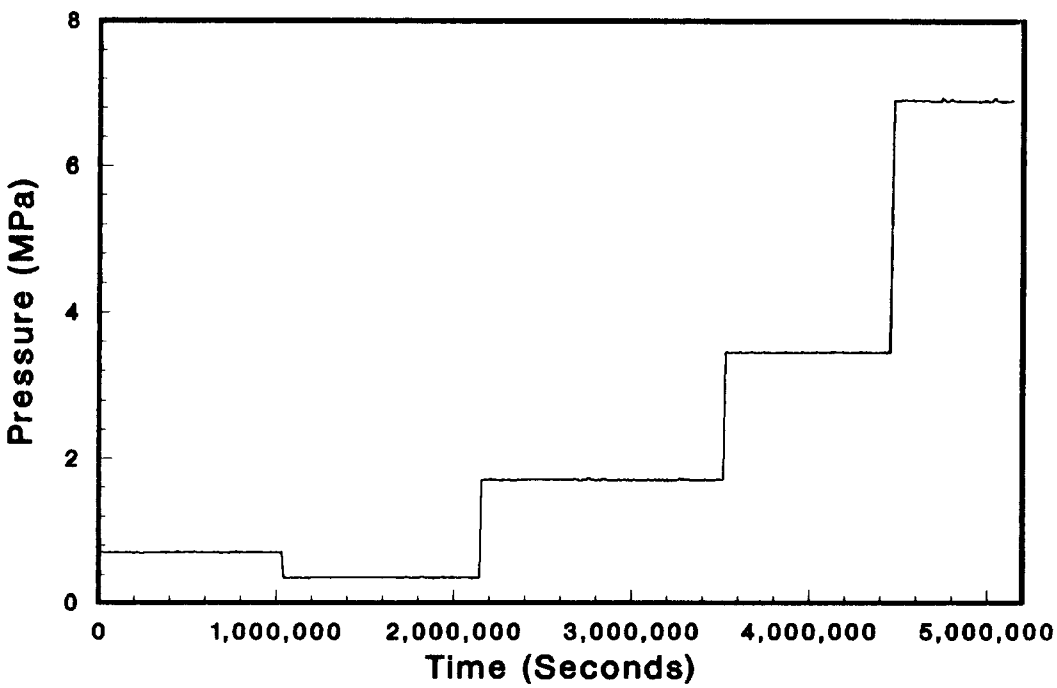

Figure 2.1. Pressure History for Test 240C61

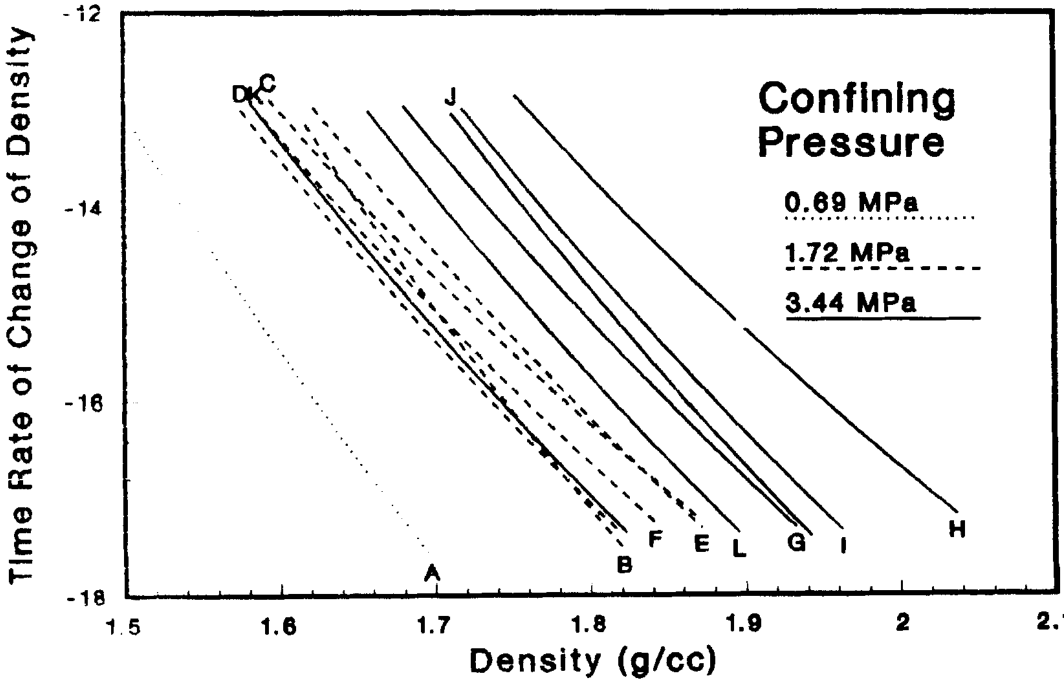

Figure 2.2. Consolidation Rate vs. Density for Hydrostatic Consolidation Tests on Wet Crushed Salt

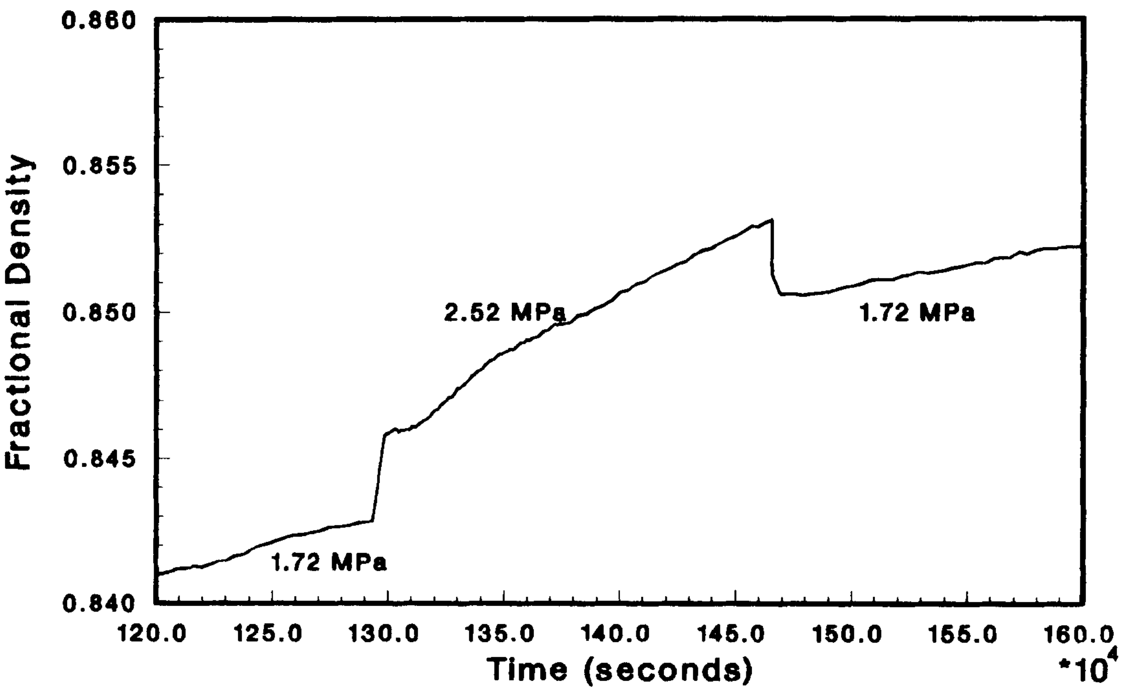

Figure 2.3. Fractional Density vs. Time for Test 23JL51

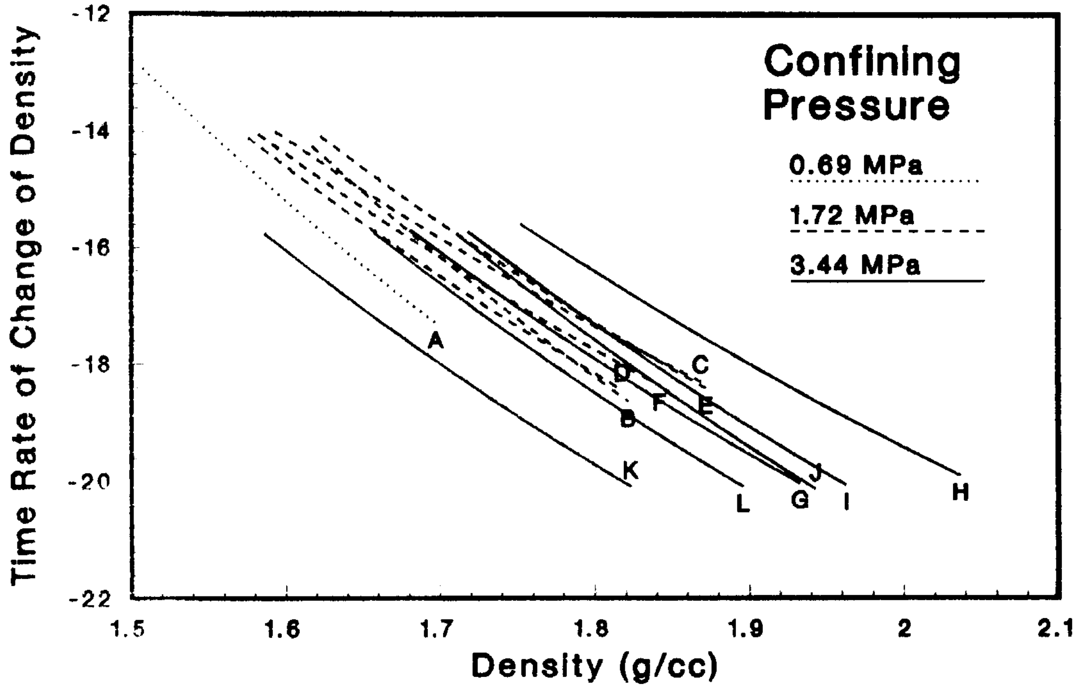

Figure 2.4. Consolidation Rate (Shifted for Pressure) vs. Density for Hydrostatic Consolidation Tests on Wet Crushed Salt

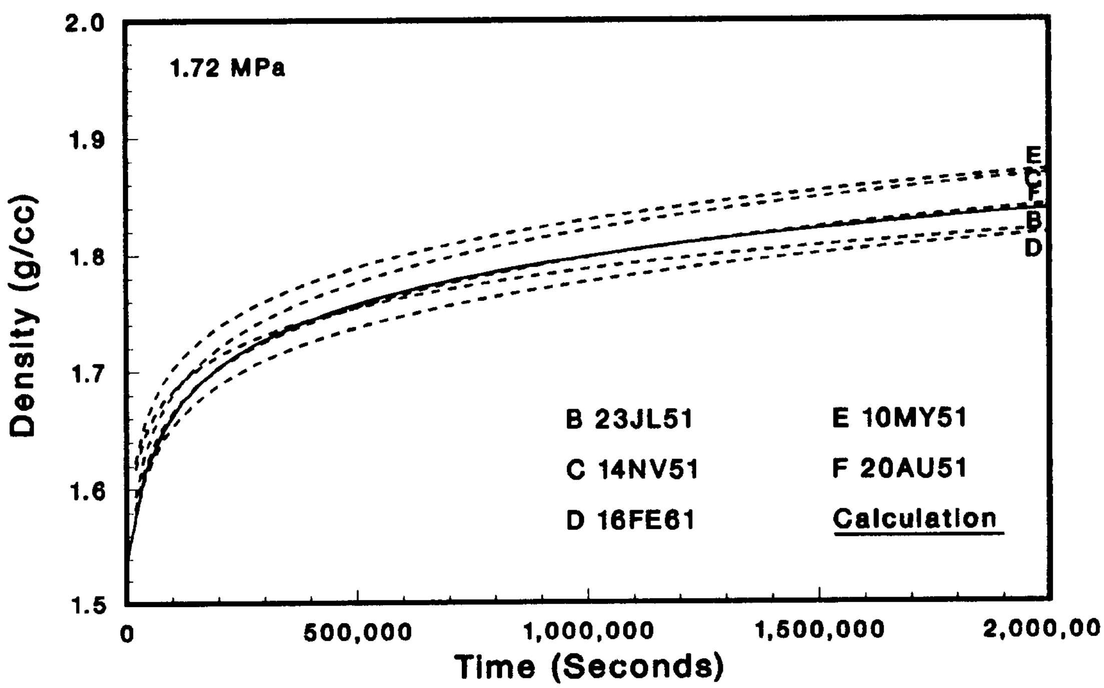

Figure 2.5. Comparison of Measured and Predicted Volumetric Creep for Confining Pressure = 1.72 MPa

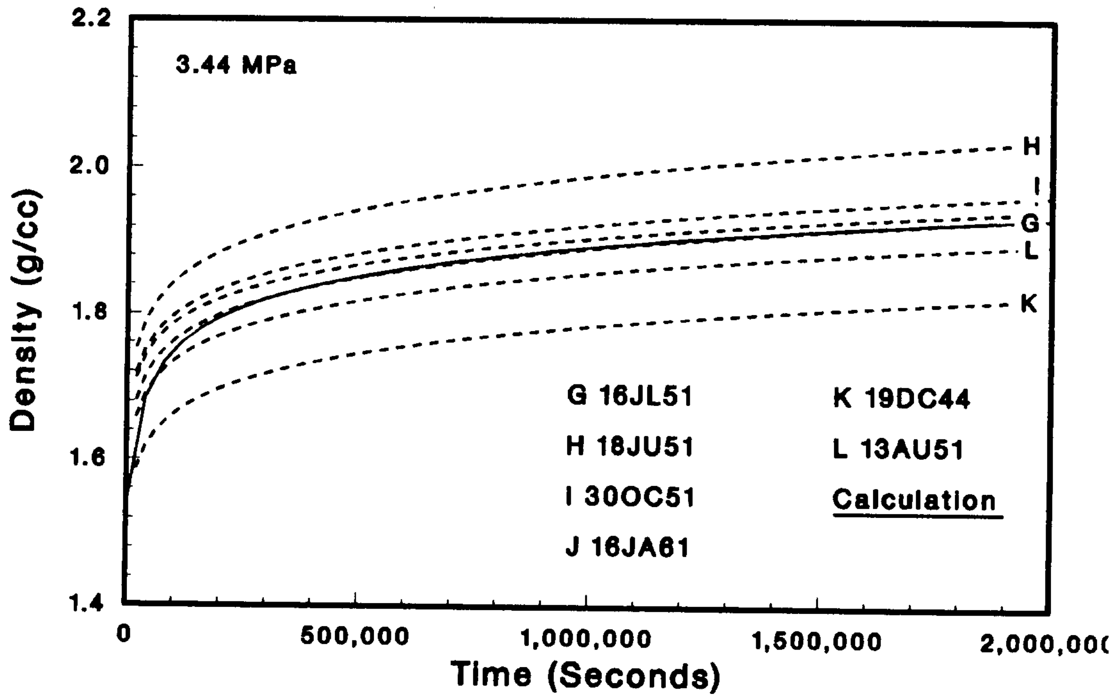

Figure 2.6. Comparison of Measured and Predicted Volumetric Creep for Confining Pressure = 3.44 MPa

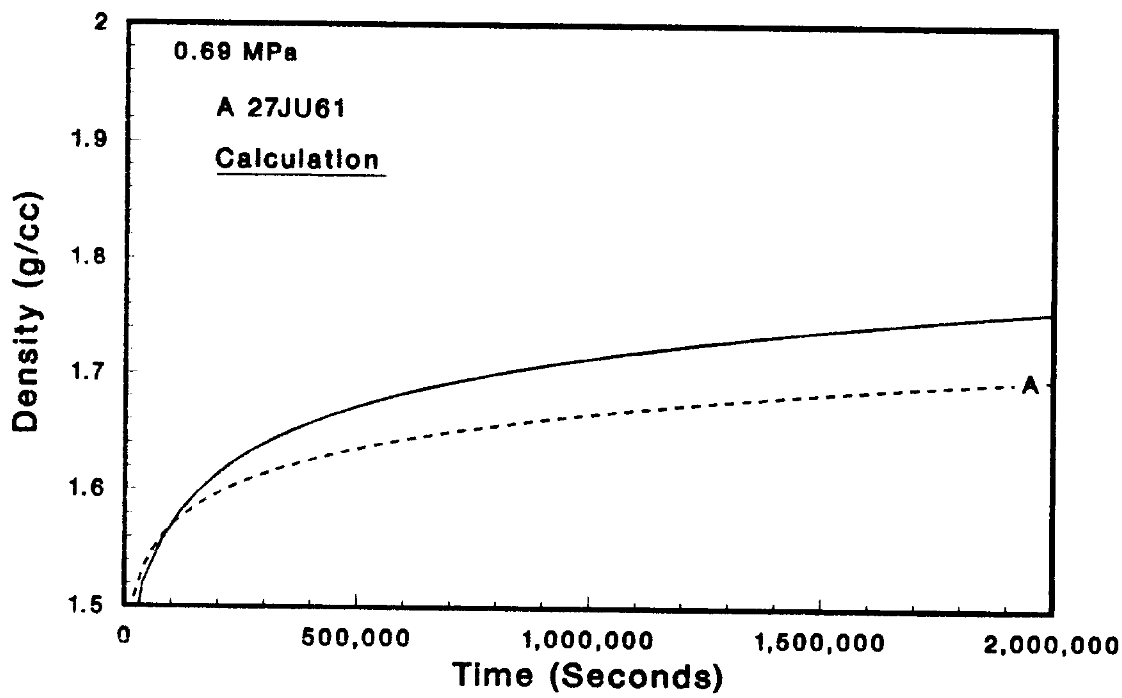

Figure 2.7. Comparison of Measured and Predicted Volumetric Creep for Confining Pressure = 0.69 MPa

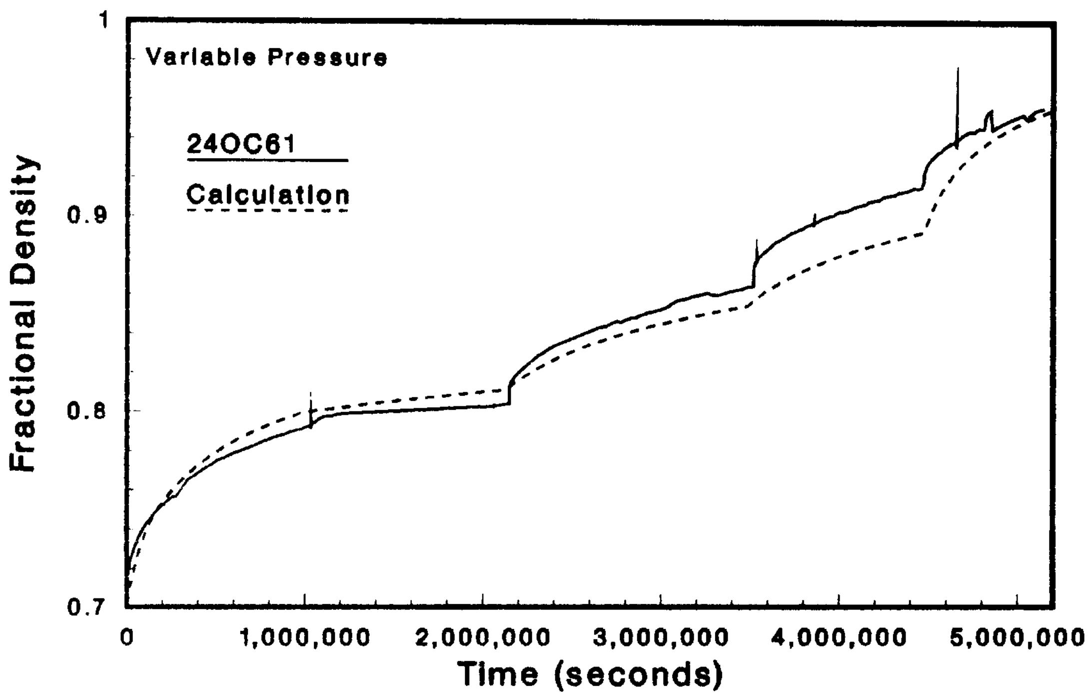

Figure 2.8. Comparison of Measured and Predicted Volumetric Creep for Variable Pressure Test 240C61

3. Constitutive Equation for Crushed Salt

This section describes the derivation of the constitutive model for crushed salt material. The model must describe an arbitrary stress state, including both volumetric and deviatoric terms. Here the volumetric behavior is assumed to be dominant because no laboratory data are presently available to describe the deviatoric behavior. The development of the deviatoric model is based entirely on judgement.

3.1 Previous Constitutive Models

Two of the more well known attempts to devise constitutive models for crushed salt are the empirical model of Ratigan and Wagner [16] and the sintering model of Zeuch, Holcomb and Lauson [24]. Both of these are based on data from tests on dry material and only describe the volumetric behavior. Ratigan and Wagner represented the creep behavior of dry crushed salt with the expression:

$$\dot{e}_{vc} = A(p/p_0)^n (T/T_0)^c (e_{vc})^{-m} \tag{3.1.1}$$

where: e_{vc} is the volumetric creep strain,
$\dot{e}_{vc}$ is the volumetric creep strain rate (1/s),
p is the pressure or mean stress (psi),
p_0 is the normalizing pressure (1450 psi),
T is the temperature (F),
T_0 is the normalizing temperature (32° F), and
A, m, n, and c are experimentally determined constants.

This expression is based on a limited amount of data and does not fit the data from the wet crushed salt tests particularly well. Zeuch, Holcomb and Lauson showed that a simple model for hot-pressing, used in the fields of ceramics and powder metallurgy to model the consolidation of powdered aggregates, fit the results of the individual creep consolidation tests in Reference [8] reasonably well. The equation is of the form

$$\frac{dD}{dt} = \frac{3P_c(1-D)}{4\eta}\left[\frac{1}{1-(1-D)^{2/3}} + \frac{\sqrt{2}\tau}{P_c}\ln(1-D)\right] \tag{3.1.2}$$

where: D is the fractional density,
t is the time,
P_c is the pressure,
η is the solid "viscosity", and
τ is the volumetric yield stress.

A limitation of this model is the prediction of a fractional endpoint density less than one. That is, the model implies that the density of intact salt may be unattainable. As shown in Reference [24] and also by McClelland in the original reference [11], setting the left side of Equation (3.1.2) to zero and solving for D_E gives

$$\left[1-(1-D_E)^{2/3}\right]\left[\ln\frac{1}{(1-D_E)}\right]=\frac{P_c}{\sqrt{2}\tau} \tag{3.1.3}$$

where D_E is the fractional endpoint density. An endpoint density less than one was a possibility based on the initial data from the dry crushed salt tests. However, the recent tests on wet crushed salt [4,14] show that creep consolidation does continue for long times to near intact densities and that the long term behavior is the phenomenon of interest so the sintering model was not developed further.

3.2 Basic Definitions and Assumptions

The current value of the stress and total strain rate are denoted by σ_{ij} and $\dot{\epsilon}_{ij}$, respectively. These are decomposed into volumetric and deviatoric parts using Equations (3.2.1)–(3.2.4):

$$P = -\tfrac{1}{3}\sigma_{kk} \tag{3.2.1}$$
$$S_{ij} = \sigma_{ij}-\tfrac{1}{3}\sigma_{kk} \tag{3.2.2}$$
$$\dot{e}_v = -\dot{\epsilon}_{kk} \tag{3.2.3}$$
$$\dot{e}_{ij} = \dot{\epsilon}_{ij}-\tfrac{1}{3}\dot{\epsilon}_{kk} \tag{3.2.4}$$

where: P is the pressure (positive in compression),
S_{ij} is the deviatoric stress,
$\dot{e}_v$ is the volumetric strain rate (positive for decreasing volume), and
$\dot{e}_{ij}$ is the deviatoric strain rate.

In most quasi-static finite element programs, the total strain rate $\dot{\epsilon}_{ij}$ is taken to be constant over a time step since higher derivatives are generally not available. For clarity the symbols r and $\dot{e}'_{ij}$ are used here to denote the constant values of the volumetric and deviatoric strain rates, respectively, at some arbitrary time step. The sub- or superscripts $()_0$ and $()_F$ will be used to denote the values of stresses and densities at the beginning and end of the time step, respectively and t will denote some instant of time within the current step. The relationships between volume strain, e_v, and density, ρ, are given in Section 2.1.

3.3 Volumetric Constitutive Model

In the previous chapter the consolidation behavior was shown to be described by Equation (2.5.2). This is written in terms of the volumetric creep strain rate as:

$$\dot{e}_{vc} = \frac{\rho_0}{\rho^2} B_0 \left[e^{B_1 P} - 1\right] e^{A\rho} \tag{3.3.1}$$

where ρ_0 is the density corresponding to zero volume strain and $\dot{e}_{vc} = \rho_0 \dot{\rho}/\rho^2$ from Equation (2.1.2). The total volumetric strain rate is written as the sum of the elastic strain rate and the creep strain rate

$$\dot{e}_v = \dot{P}/K + \dot{e}_{vc}$$

where $\dot{P}$ is the rate of change of the pressure and K is the elastic bulk modulus. Equation (3.3.1) is substituted into the above equation and the result restated as:

$$\dot{P} = K\left(\dot{e}_v - \frac{\rho_0}{\rho^2} B_0 \left[e^{B_1 P} - 1\right] e^{A\rho}\right) \tag{3.3.2}$$

The bulk modulus is approximated by an exponential function of density that can be expressed as (see Appendix A):

$$K = K_0 e^{K_1 \rho} \tag{3.3.3}$$

where K_0 and K_1 are constants determined from a fitting procedure. The density terms appearing in the expression for the bulk modulus and in the term $e^{A\rho}$ in Equation (3.3.2) are expressed in terms of the volume strain using Equation (2.1.3).

$$K_0 e^{K_1 \rho} \approx K_0 e^{K_1 \rho_0 (1+e_v)} \tag{3.3.4}$$

$$e^{A\rho} \approx e^{A\rho_0(1+e_v)} \tag{3.3.5}$$

The term ρ_0/ρ^2 in Equation (3.3.2) is expressed in terms of the volume strain using Equation (2.1.3)

$$\rho_0/\rho^2 = (1 - e_v)^2/\rho_0 \tag{3.3.6}$$

Using Equations (3.3.4), (3.3.5), and (3.3.6), Equation (3.3.2) can be written as

$$\dot{P} \approx K_0 e^{K_1 \rho_0 (1+e_v)} \left\{\dot{e}_v - \frac{(1 - e_v)^2}{\rho_0} B_0 \left[e^{B_1 P} - 1\right] e^{A\rho_0(1+e_v)}\right\} \tag{3.3.7}$$

which is the constitutive equation relating the rate of change of the pressure to the volumetric strain rate and density.

3.3.1 Integration of the Volumetric Constitutive Equation

To integrate this expression in a quasi-static finite element program, $\dot{e}_v$ over a time step is approximated by the constant value r because higher derivatives are generally not available. Using this approximation,

$$\dot{e}_v = r \tag{3.3.8}$$

$$e_v = e_{v0} + rt \tag{3.3.9}$$

where e_{v0} is the volume strain at the beginning of the time step and t is the length of the time step. Since Equations (2.5.2) and (3.3.3) depend only on the current value of the density, the volume strain at the beginning of the time step can be set to zero and then ρ_0 is the density at the beginning of the time step. The volume strain at the end of the time step is then given by rt and the density by

$$\rho = \rho_0/(1 - rt) \approx \rho_0(1 + rt) \tag{3.3.10}$$

Equation (3.3.7) is rewritten in terms of r to give the following first-order nonhomogeneous nonlinear ordinary differential equation for the pressure:

$$\dot{P} = K_0 e^{K_1\rho_0(1+rt)} \left\{ r - \frac{(1-rt)^2}{\rho_0} B_0 \left[e^{B_1 P} - 1 \right] e^{A\rho_0(1+rt)} \right\} \tag{3.3.11}$$

If $rt < 0.1$, then the quantity $(1 - rt)^2$ can be approximated as e^{-2rt} with an error of less than one percent and Equation (3.3.11) can be written as

$$\dot{P} = \frac{\hat{K} e^{\beta t}}{B_1} - \frac{\hat{B} e^{\alpha t} e^{B_1 P}}{B_1} + \frac{\hat{B} e^{\alpha t}}{B_1} \tag{3.3.12}$$

where:
$$\begin{aligned} \hat{K} &= B_1 K_0 r e^{K_1 \rho_0}, \\ \hat{B} &= B_1 B_0 K_0 e^{\rho_0(A+K_1)}/\rho_0, \\ \beta &= K_1 \rho_0 r, \\ \alpha &= (K_1\rho_0 + A\rho_0 - 2)\, r. \end{aligned}$$

A change of variables is used in the form:

$$w = e^{-B_1 P} \qquad \text{and} \qquad \dot{w} = -B_1 \dot{P} w$$

which are substituted into Equation (3.3.12) to obtain an equation linear in w:

$$\dot{w} + \hat{K} e^{\beta t} w + \hat{B} e^{\alpha t} w = \hat{B} e^{\alpha t} \tag{3.3.13}$$

This equation has the solution:

$$w = e^{-I} \int \hat{B} e^{\alpha t} e^{I}\, dt + C e^{-I}$$

where:

$$I = \int (\hat{K} e^{\beta t} + \hat{B} e^{\alpha t})\, dt = \frac{\hat{K} e^{\beta t}}{\beta} + \frac{\hat{B} e^{\alpha t}}{\alpha}$$

so that:

$$\begin{aligned} w(t) = {} & \hat{B} \exp\left(-\frac{\hat{K} e^{\beta t}}{\beta} - \frac{\hat{B} e^{\alpha t}}{\alpha} \right) \int e^{\alpha t} \exp\left(\frac{\hat{K} e^{\beta t}}{\beta} + \frac{\hat{B} e^{\alpha t}}{\alpha} \right) dt \\ & + C \exp\left(-\frac{\hat{K} e^{\beta t}}{\beta} - \frac{\hat{B} e^{\alpha t}}{\alpha} \right) \end{aligned} \tag{3.3.14}$$

where C depends on the initial conditions. To complete the integration note that if αt and βt are less than approximately 0.1 the following approximation can be used with less than a one percent error.

$$e^{\gamma} \approx 1 + \gamma \tag{3.3.15}$$

Using this approximation, the integral in Equation (3.3.14) is approximated as:

$$\begin{aligned}
\int \exp\left(\alpha t + \frac{\hat{K}e^{\beta t}}{\beta} + \frac{\hat{B}e^{\alpha t}}{\alpha}\right) dt &\approx \int \exp\left[\alpha t + \frac{\hat{K}}{\beta}(1+\beta t) + \frac{\hat{B}}{\alpha}(1+\alpha t)\right] dt \\
&= \exp\left(\frac{\hat{K}}{\beta} + \frac{\hat{B}}{\alpha}\right)\int e^{(\alpha+\hat{K}+\hat{B})t}\, dt \\
&= \frac{e^{(\alpha+\hat{K}+\hat{B})t}}{\alpha+\hat{K}+\hat{B}} \exp\left(\frac{\hat{K}}{\beta} + \frac{\hat{B}}{\alpha}\right) \qquad (3.3.16)
\end{aligned}$$

Using Equations (3.3.15) and (3.3.16), Equation (3.3.14) is written as:

$$w(t) = \frac{\hat{B}e^{\alpha t}}{\alpha+\hat{K}+\hat{B}} + C\exp\left(-\frac{\hat{K}e^{\beta t}}{\beta} - \frac{\hat{B}e^{\alpha t}}{\alpha}\right) \tag{3.3.17}$$

At time $t = 0$:

$$w(0) = \frac{\hat{B}}{\alpha+\hat{K}+\hat{B}} + C\exp\left(-\frac{\hat{K}}{\beta} - \frac{\hat{B}}{\alpha}\right)$$

which can be solved for C giving

$$C = \left[w(0) - \frac{\hat{B}}{\alpha+\hat{K}+\hat{B}}\right]\exp\left(\frac{\hat{K}}{\beta} + \frac{\hat{B}}{\alpha}\right)$$

Changing back to the original variables and solving for the pressure, Equation (3.3.17) is written as:

$$P_F = \frac{-\ln}{B_1}\left\{\frac{\hat{B}e^{\alpha t}}{\alpha+\hat{K}+\hat{B}} + \left[e^{-B_1P_0} - \frac{\hat{B}}{\alpha+\hat{K}+\hat{B}}\right]\exp\left\{\frac{\hat{K}}{\beta}(1-e^{\beta t}) + \frac{\hat{B}}{\alpha}(1-e^{\alpha t})\right\}\right\} \tag{3.3.18}$$

or, using Equation (3.3.15) to approximate the exponential terms $e^{\alpha t}$ and $e^{\beta t}$, the final form of the constitutive equation modeling the volumetric consolidation of crushed salt is:

$$P_F = \frac{-\ln}{B_1}\left\{\frac{\hat{B}(1+\alpha t)}{\alpha+\hat{K}+\hat{B}} + \left[e^{-B_1P_0} - \frac{\hat{B}}{\alpha+\hat{K}+\hat{B}}\right]\exp\left\{-t(\hat{K}+\hat{B})\right\}\right\} \tag{3.3.19}$$

where: A, B_0, B_1, K_0, K_1 are material constants,

P_0 = is the pressure at the beginning of the time step,

r = is the volumetric strain rate during the time step,

$\hat{B}$ = $B_0 B_1 K_0 e^{\rho_0 (A+K_1)} / \rho_0$

$\hat{K}$ = $B_1 K_0 r e^{K_1 \rho_0}$

α = $(K_1 \rho_0 + A\rho_0 - 2)r$

β = $K_1 \rho_0 r$

And the following assumptions were used:

$$\alpha t, \quad \beta t, \quad rt \quad \begin{cases} < 0.5 & \text{for} < 10\% \text{ error} \\ < 0.1 & \text{for} < 1\% \text{ error} \end{cases} \tag{3.3.20}$$

3.4 Deviatoric Constitutive Model

The previous section documented the derivation of the equation modeling the volumetric behavior of crushed salt material. The constitutive model must also model the deviatoric or shear behavior. At the current time, no tests which isolate the deviatoric behavior of crushed salt have been performed. The development reported in this section is therefore based totally on judgement.

Four models that could be used to model the deviatoric response of crushed salt are, in order of increasing complexity:

- Elastic,
- Elastic–Plastic,
- Elastic–Creep, and
- Elastic–Plastic–Creep.

The equations describing each of these, except for an *Elastic–Plastic–Creep* model, will be presented below. A more detailed deviatoric model will be developed when the correct deviatoric behavior of crushed salt is determined.

3.4.1 Elastic Deviatoric Model

The elastic deviatoric model can be written as

$$S_{ij}^F = S_{ij}^0 + 2G_\rho \dot{e}'_{ij} t \tag{3.4.1}$$

where G_ρ is the elastic shear modulus evaluated at some density within the time step and t is the length of the time step. Though this model is easily implemented, it is known that the deviatoric behavior of crushed salt is not elastic because intact salt is a deviatorically creeping material. The crushed salt behavior should approach intact behavior as the density approaches intact density. An elastic deviatoric model does have some merit, though, if it is used for parametric studies and in analyses seeking to bound the crushed salt response.

3.4.2 Elastic–Plastic Deviatoric Model

The elastic–plastic deviatoric model used here is based on a standard von Mises type yield condition with no hardening. Initially a trial stress S_{ij}^T is calculated assuming that no plasticity occurs during the time step

$$S_{ij}^T = S_{ij}^0 + 2G_\rho \dot{e}'_{ij} t \tag{3.4.2}$$

The magnitude of the trial deviatoric stress is then calculated as

$$S^T = \sqrt{S_{ij}^T S_{ij}^T} \tag{3.4.3}$$

and then compared to the yield stress σ_Y to determine if yield occurs. The variable κ is used to define the yield von Mises yield surface.

$$\kappa = \sqrt{\tfrac{2}{3}}\,\frac{\sigma_Y}{S^T} \tag{3.4.4}$$

The final deviatoric stress state S_{ij}^F is then calculated from this value of κ. If the value of κ is greater than 1, then the assumption of no plasticity is correct and the trial stress state is the final stress state; if κ is less than 1, then plastic deformation has occurred and the final stress state must be reduced.

$$S_{ij}^F = \begin{cases} S_{ij}^T & \text{if } \kappa \geq 1 \\ \kappa S_{ij}^T & \text{if } \kappa < 1 \end{cases} \tag{3.4.5}$$

This model is more appropriate than the elastic model because the yield stress σ_Y can be a function of density which more accurately models the stiffening behavior of crushed salt with increasing density. Like the elastic model, the elastic-plastic model is also very easily implemented. However, it does not accurately model the behavior of crushed salt in the limit as the density approaches intact salt density because it does not account for deviatoric creep.

3.4.3 Elastic–Creeping Model

Because intact salt creeps when subjected to a deviatoric stress state, crushed salt should logically be expected to creep deviatorically. This expectation becomes increasingly more reasonable as the density increases because, in the limit, the crushed salt becomes intact salt. The deviatoric crushed salt creep model presented here is based on a secondary creep model which has been used to describe the secondary creep behavior of intact WIPP salt [10].

The development proceeds by envisioning that the porous crushed salt uniaxial sample is composed of cylinders of salt, each of which has the intact salt secondary creep behavior separated by areas of open space. The local stress acting on the salt cylinders is then stated in terms of the average stress on the porous sample. The cross-sectional area of the porous sample is expressed in terms of the net cross-sectional area of the salt cylinders. This implied areal ratio is the inverse of the fractional density of the sample. The final resulting continuum model for the rate of the deviatoric stress of crushed salt is then

$$\dot{S}_{ij} = 2G_\rho \left(\dot{e}'_{ij} - A(\rho_\infty/\rho)^n e^{(Q/RT)} \left|S_{pq}\right|^{n-1} S_{ij}\right) \tag{3.4.6}$$

where the material constants A, Q, n, and ρ_∞ refer to the values for intact salt [10]. This expression for the deviatoric stress rate is a stiff equation in the mathematical sense and must be implemented into a computer program with some care. A semi-analytical method developed for intact salt [9] and used in the structural analyses for the WIPP project [20] is used to integrate Equation (3.4.6). In the limit of no void volume, this model reduces to the elastic–secondary creep model for intact rock salt. The actual behavior is probably a unified combination of the creep and plasticity model with each behavior dominating the response in different density ranges.

3.5 Summary of the Constitutive Model

The volumetric behavior modeled by Equation (3.3.19) and the deviatoric behavior modeled by Equations (3.4.1), (3.4.5), and (3.4.6) have been implemented in the quasistatic, large deformation finite element program, SANCHO [20]. All three deviatoric models were implemented to aid in studies of the effect of the deviatoric behavior on the overall response of the material. Any of the three deviatoric models can be selected prior to the calculation. The instructions for using this model in SANCHO are documented in Appendix B.

The constitutive subroutine is entered with the current value of the total strain rate $\epsilon ij'$, the stress state from the end of the previous time step σ^0_{ij}, and the density from the end of the previous time step ρ_0. The stress and strain rate are then decomposed into the volumetric and deviatoric parts using Equations (3.2.1)–(3.2.4). The volumetric response is then calculated using Equation (3.3.19) to calculate P_F and Equation (3.3.10) to calculate ρ_F. A subiteration scheme ensures that the approximations of Equation (3.3.20) are satisfied.

The deviatoric response is then calculated using the selected model. Although the shear modulus is a function of the density ρ which changes throughout the time step, all of the deviatoric models are currently written in terms of a G which is constant over the time step. This was done simply because the extra complexity required to have G vary over the time step was not judged to be warranted based on the scarcity of data describing the deviatoric behavior. The shear modulus used in the calculations is calculated using Equation (A.2) and the average density ρ_A which is defined to be $(\rho_0 + \rho_F)/2$. The final deviatoric stress state S_{ij}^F is calculated using this value of G and either Equation (3.4.1), (3.4.5), or (3.4.6).

The final total stress state is then obtained by recomposing the volumetric and deviatoric stresses.

$$\sigma_{ij}^F = S_{ij}^F - \delta_{ij} P_F \tag{3.5.1}$$

Several calculations performed using this model are documented in Chapter 4. Included in these are scoping calculations performed to determine the influence and importance of the deviatoric behavior to the overall response of the material. Only the elastic-plastic deviatoric model is used in these calculations because the material parameters for the elastic-creep model could not be easily determined.

4. Analyses using the Crushed Salt Constitutive Model

This chapter presents the results of several analyses performed using the crushed salt constitutive model in the finite element code SANCHO. Both single element analyses involving only crushed salt and analyses involving the interaction of intact and crushed salt in realistic configurations are presented. Several shaft calculations are performed to investigate the importance of the deviatoric behavior of crushed salt to the overall response of the closure of rooms and shafts. In these calculations, the deviatoric part of the model has been varied from the stiffest possible to the softest possible shear behavior and the differences in the closure of the analyzed shaft are compared. This chapter also includes a section describing a method used to artificially accelerate the creep of intact salt so that more realistic backfill-intact salt interactions can be obtained.

4.1 Single Element Analyses

Several single element calculations were performed to verify the implementation of the crushed salt constitutive model in SANCHO. These calculations involved the numerical simulation of the consolidation tests performed by Holcomb and Shields [4]. The finite element model consists of a single axisymmetric element loaded with a hydrostatic pressure. The hydrostatic pressure was held constant in all analyses except for the simulation of the 240C61 test where the actual pressure history shown in Figure 2.1 was used. The results from these analyses are identical to those calculated directly from the expressions in Chapter 2 and shown in Figures 2.5–2.8.

4.2 Shaft Analyses

Several calculations were performed to study the interaction between intact salt and crushed salt in realistic field configurations. The shaft configuration is the simplest configuration that can be used to study this interaction. The axisymmetric strip shown in Figure 4.1 is used to represent the shaft. The outer boundary of the strip is a distance of 200 radii from the inner boundary which is far enough to be considered an infinite boundary for the problem time span reported here. The inner radius of the shaft is 1.829 meters (6.0 feet). The borehole pressure is zero for the unbackfilled shaft. The crushed salt causes a changing borehole pressure in the backfilled shaft analyses. The elastic-secondary creep model with reduced elastic constants is used for the intact salt.

In calculations that simulate the interaction between intact salt and crushed salt, the deformation of the intact salt produces the loading in the crushed salt. To provide accurate information about the crushed salt response, the response of the intact salt must be calculated correctly. At the current time analyses of the closure rate of drift configurations at the WIPP underpredict the measured rate by approximately a factor of three [13]. A new constitutive model for intact salt may resolve the factor of three discrepancy, but such a model is, at best, in the development stage. A temporary method for increasing the creep rate of the intact salt was needed for these, and other, engineering calculations. This method is described below.

4.2.1 Accelerated Creep of Intact Salt

Morgan, *et al*, [13] investigated several possible causes for the discrepancy between the measured and computed responses of the South Drift. It was shown that reducing the elastic constants of the intact salt (halite) resulted in increased closure rates and hence closures. This study also showed that the closure histories resulting from calculations performed using the reduced elastic moduli had shapes very similar to the closure histories of data from the South Drift. Although reductions in the elastic constants of halite result in the desired increases in closure, the reason for these increased closures during the creep phase of the calculation is not readily apparent. Furthermore, reductions in the elastic constants are difficult to justify on physical grounds. The reference values of the elastic constants represent the unloading and reloading slopes of axial stress—axial strain curves obtained in laboratory tests on halite samples and are in good agreement with elastic constants determined from sound speeds measured in ultrasonic tests [23].

In Reference [13], physically based causes for the discrepancy between measured and calculated closures and closure rates were being explored. Therefore, because no physical basis for modifying the elastic constants existed, the subject was not pursued further in that study. In the current study, emphasis is placed on the behavior of crushed salt rather than intact salt so any method for computing closure rates of the same magnitude as the measurements is appropriate until the time that a more accurate material model is developed for the behavior of intact salt. Because reducing the elastic constants was shown to both increase the closure rate and to very closely match the shape of the closure history data from the South Drift, this approach was used for the crushed salt—intact salt interaction calculations presented here.

The factor by which the elastic constants were reduced was found by trial and error. A reference shaft closure history was calculated using the reference elastic constants. The elastic constants were then divided by a trial factor and the calculation repeated. This process was continued until closure rates computed with the reduced moduli were approximately three times the closure rates computed with the reference moduli. The closure rates were compared at a time corresponding to approximately 1200 days after excavation which corresponds to the latest South Drift closure data available at that time. Measured closure rates for the South Drift were 3 times larger than the computed rates. Furthermore, the behavior of a shaft is similar to that of a drift. Hence, the procedure involved trying to increase shaft closure rates by a factor of 3 over the reference closure rates. Dividing both the elastic bulk and shear moduli by a factor of 12.5 resulted in the desired increase in closure rate. Figure 4.2 shows the closure rates for both the reference and reduced analyses, and Figure 4.3 shows the respective closure histories. Also shown in these figures are the data for the E140-S1246 closure station in the South Drift at the WIPP [15].

The 12.5 reduction factor has since been used in several calculations which have shown that the agreement between calculated and measured closures is fairly good; the method slightly underestimates the vertical closure and very closely estimates the horizontal closure when applied to drift configurations. Unless otherwise noted, all of the calculations described below use the reduced elastic moduli for the intact salt properties. The WIPP reference values [10] are used for the secondary creep parameters.

4.2.2 Baseline Shaft Analysis

A long term shaft analysis was performed to provide a baseline closure rate for comparison with the backfilled shaft calculations. In this analysis, which will be referred to as the baseline analysis, the shaft opening is not filled with crushed salt. The analysis simulates the closure of a 1.829 meter radius shaft at a depth of approximately 640 meters for a time of 4,000 years. Figure 4.4 is a plot of the normalized closure vs. time and Figure 4.5 shows the same curve on a logarithmic scale plot. The normalized closure is calculated by dividing the radial closure by the original shaft radius. The closure rate is plotted vs. time in Figure 4.6.

4.2.3 Backfilled Shaft Analyses

The crushed salt constitutive model was used in several calculations involving the simulation of the closure of a cylindrical shaft backfilled with wet crushed salt. The results of these calculations were compared with the closure of the baseline unbackfilled shaft to determine how much the consolidating backfill material slowed the closure rate of the intact salt.

The first pair of analyses was performed to determine the effect of the crushed salt on the closure rate and also to determine the importance of the deviatoric behavior of the crushed salt. The borehole contained wet crushed salt backfill material at an initial density of 1.70 g/cc (80% fractional density) in both of these analyses; the only difference was the modeling of the deviatoric behavior. In one case the crushed salt was modeled as having no shear strength by setting the shear modulus to a very low value. This is a lower bound on the shear behavior of the material. The upper bound on the shear strength for the borehole configuration occurs when the circumferential and axial stress in the backfill are both zero. The only non-zero stress component is the radial stress. This provides the maximum magnitude of the deviatoric stress for a given value of the mean stress. Both cases were run for a period of 100 years (3.156×10^9 seconds). Figure 4.7 shows the normalized closure computed for each case and the baseline analysis. These results show that the wet crushed salt backfill material does not significantly retard the closure rate of the intact salt. The results for the two deviatoric models are also nearly identical which indicates that at the slow closure rates seen in realistic configurations the volumetric behavior of the crushed salt dominates the overall response of the material. As the density of the crushed salt material increases to near intact densities, deviatoric behavior will become important. However, no materials test data are currently available to describe this transition from a consolidating material to an intact material and the constitutive model is not designed to model this behavior accurately. The maximum fractional density reached during the materials testing was approximately 90%; the material behavior above this value is extrapolated.

The second set of analyses was performed to determine the effect of the emplacement density of the crushed salt backfill on the closure rate of the intact salt. Five analyses were run with initial densities ranging from 1.70 g/cc to 1.95 g/cc in increments of 0.50 g/cc (80% to 91% fractional density). Figure 4.8 is a plot of the fractional density vs. time for each of the analyses and Table 4.1 shows the time required for the backfill material to reach 95% and 100% of intact density. Note that the consolidation rate is nonzero when the fractional density is equal to 1. This is caused by deriving the constitutive model from Equations (2.2.1) and (2.3.1) which are empirical equations based on a limited amount of data that did not approach intact density. This provides another indication that the constitutive model should not be used to predict the behavior of crushed salt at densities above approximately 95% until more relevant data are available.

Figure 4.9 shows the ratio of the current density to the initial density for each of the analyses. Also shown is an equivalent value for the baseline shaft based upon the volume change of the shaft. The ratio ρ/ρ_0 is equal to $(1 - e_v)^{-1}$ where e_v, the volume strain, is equal to the change of shaft area divided by the original shaft area. Figure 4.10 shows the time derivative of the density ratio. From this figure it can be seen that the crushed salt provides very little resistance to closure of the shaft until the density approaches intact density. The time required for consolidation of the crushed salt material to various densities can be estimated fairly closely from the closure calculated from an unbackfilled shaft analysis.

4.3 Drift Analyses

In the previous section it was shown that the crushed salt provided very little resistance to the closure of the intact salt in the shaft configuration. In this section the interaction between the crushed salt and intact salt in a drift configuration will be investigated.

The initial drift configuration used in the interaction investigations is an array of drifts 5.03 m wide by 4.0 m high and spaced 40.54 m apart. The floor of the drifts are approximately 650 m below the surface. The finite element mesh used in the calculations is shown in Figure 4.11. Figure 4.12 shows a close-up view of the drift region. An all salt stratigraphy was used with the elastic moduli divided by 12.5 to provide the artificially accelerated creep rate. Reference [12] contains a full description of this configuration.

Figures 4.13 and 4.14 show the deformed shapes in the drift region at 20 and 50 years, respectively, for an unbackfilled drift. The horizontal and vertical closure are shown in Figure 4.15. The horizontal closure is equal to twice the horizontal displacement of point H in Figure 4.12 and the vertical closure is equal to the change in room height at the vertical centerline of the room.

The above analysis was then rerun with crushed salt in the drift. The crushed salt was emplaced with a density of 1.8 g/cc ($\approx$85% intact density). A close-up view of the finite element mesh around the drift is shown in Figure 4.16. Slidelines were used between the crushed salt and the intact salt to allow for separation of the two materials. There is a slight gap between the crushed salt and the intact salt at the wall and roof to allow for the initial elastic deformation of the intact salt. If this gap were not provided, the crushed salt would experience an instantaneous loading due rather than the more gradual loading due only to the creep of the intact salt. The size of the gap was determined from the elastic deformation calculated in the open drift calculation. A stiff elastic-plastic deviatoric behavior was used for this analysis. The yield strength of the crushed salt for each element at each timestep was chosen such that the maximum deviatoric stress was produced subject to the constraint that none of the stress components were tensile if the calculated pressure was compressive (see Appendix C). The analysis was run for a period of 20 years (6.312×10^8 seconds).

Figures 4.17 and 4.18 show the deformed shape at 10 and 20 years, respectively; the closure histories for the backfilled drift are compared to those of the open drift in Figure 4.19. The closure histories are very similar at early times. The closure history of the backfilled drift begins to deviate from the unbackfilled closure history when the density in the backfill exceeds approximately 90–95% fractional density.

Contour plots of the crushed salt fractional density are shown at 10 and 20 years in Figures 4.20 and 4.21, respectively. At 20 years the majority of the crushed salt has consolidated to greater than 95% of intact density except for at the top and bottom corners of the drift. The salt at these locations has been squeezed out of the corners leaving areas of unconsolidated crushed salt. Since the area around the room is fairly coarsely meshed, one hypothesis was that these unconsolidated areas were artifacts of the modeling and would not appear in a more finely meshed analysis.

To test this hypothesis, a second drift analysis was run. A close-up of the finite element mesh around the room is shown in Figure 4.22. This mesh has rounded corners to more accurately model the actual configuration and is more finely meshed to hopefully smooth out the piece-wise linear deformation pattern apparent in the previous calculation. The room dimensions for this analysis were changed to a width of 3.2 m and a height of 4.3 m based on information about the actual field configuration that was obtained subsequent to the previous calculation. Figures 4.23 and 4.24 show the deformed shape of the unbackfilled drift at 20 and 49 years, respectively. Although the pinching at the corners is not nearly as pronounced as in the square corner analysis, it still exists. Another reason for the reduction of the pinching effect is the reduction of the horizontal span of the room which reduces the vertical deformation.

An analysis of a similar configuration with crushed salt backfill material in the room was unsuccessful due to problems with the slidelines near the corners of the room.

As was stated earlier, the deviatoric yield strength was chosen such that the maximum deviatoric stress was produced subject to the constraint that none of the stress components were tensile. This was done to maximize the shear stiffness of the backfill material and also to determine numerically the maximum theoretically possible value of the yield stress as a function of the density assuming that the crushed salt can be modeled with an elastic-plastic deviatoric model. The procedure used for these analyses is described in Appendix C.

Table 4.1. Consolidation Times for Backfilled Shaft Analyses

Initial Density (g/cc)	*Years to Density 95%*	*Years to Density 100%*
1.70	35	58
1.75	27	49
1.80	20	41
1.85	14	33
1.90	9	25
1.95	5	19

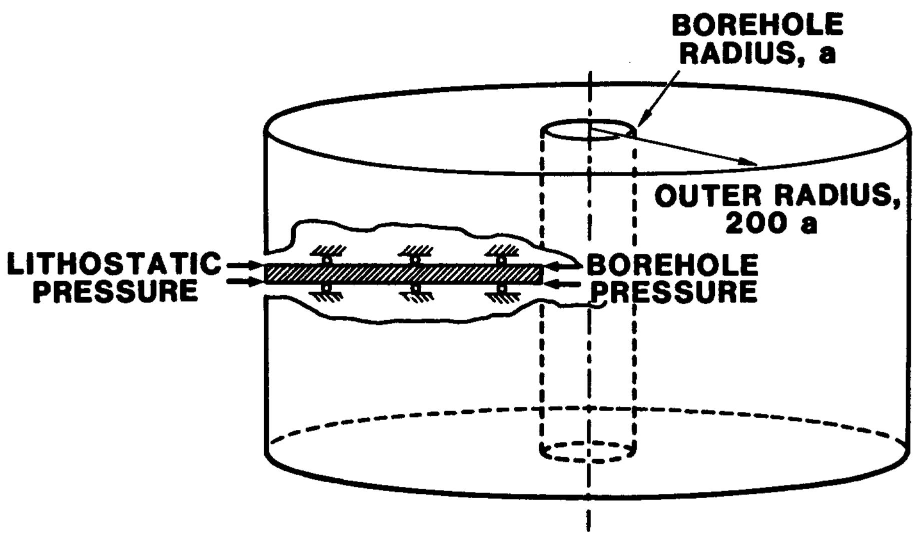

Figure 4.1. Shaft Configuration

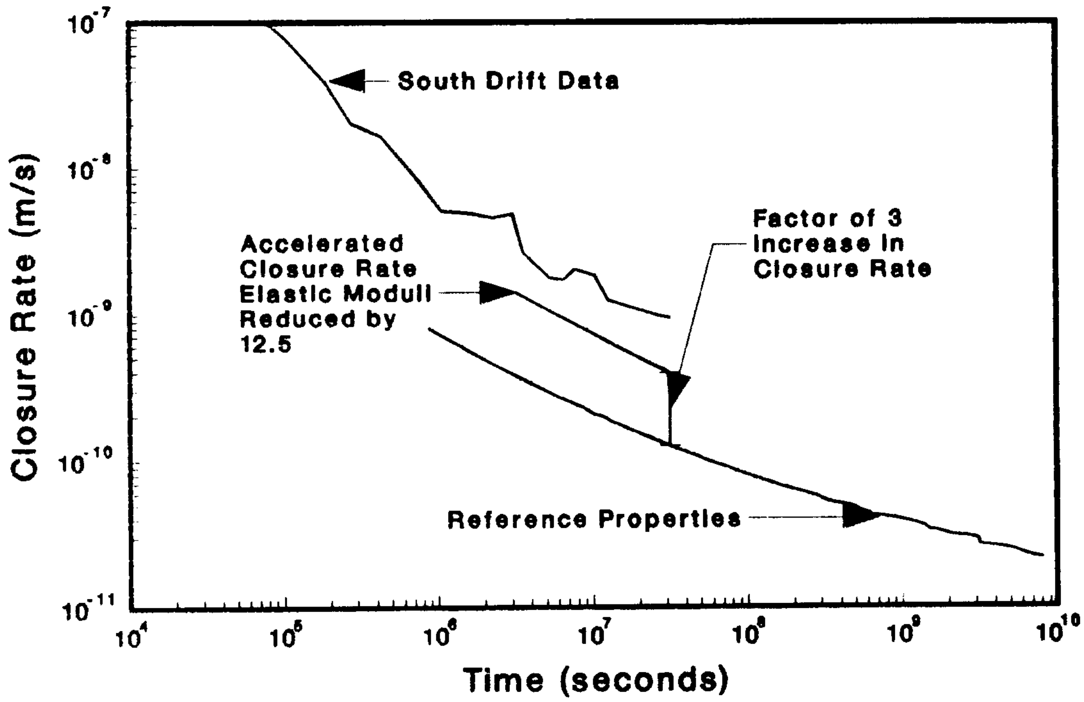

Figure 4.2. Comparison of Closure Rates for Reference and Reduced Moduli Shaft Analyses

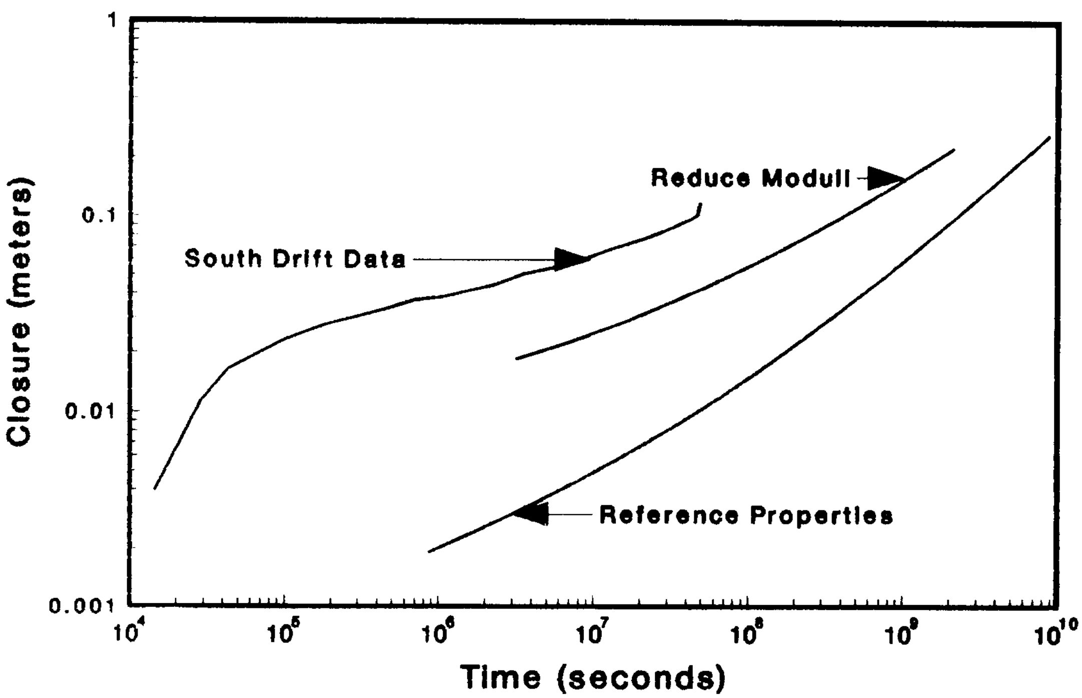

Figure 4.3. Comparison of Closure for Reference and Reduced Moduli Shaft Analyses

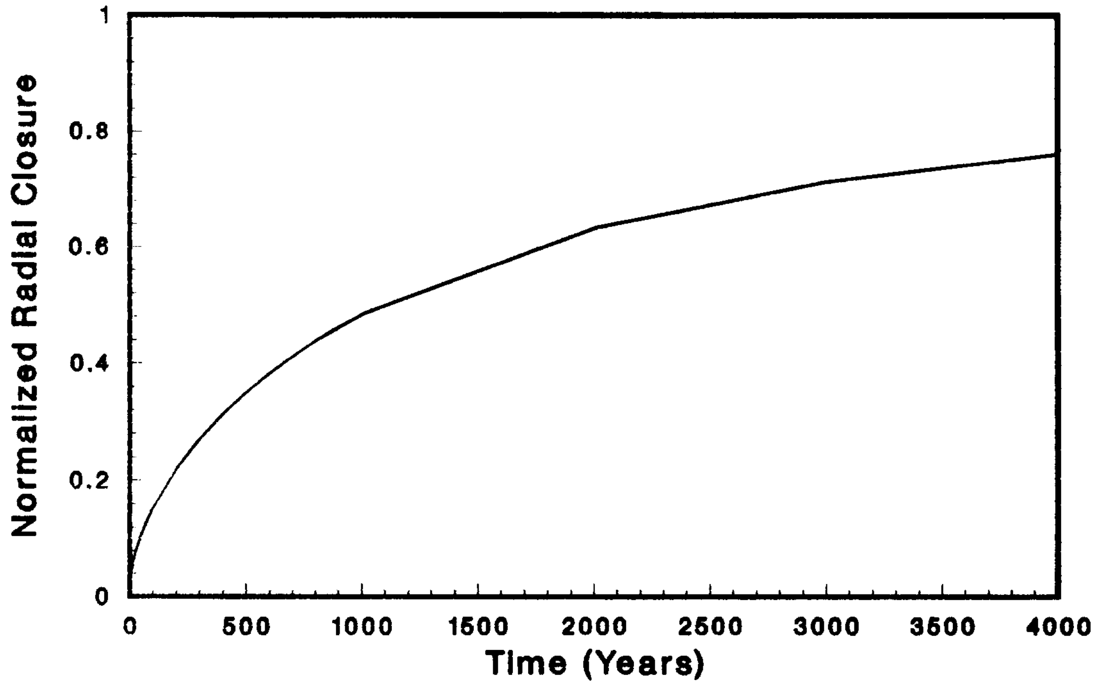

Figure 4.4. Normalized Closure History for Baseline Shaft

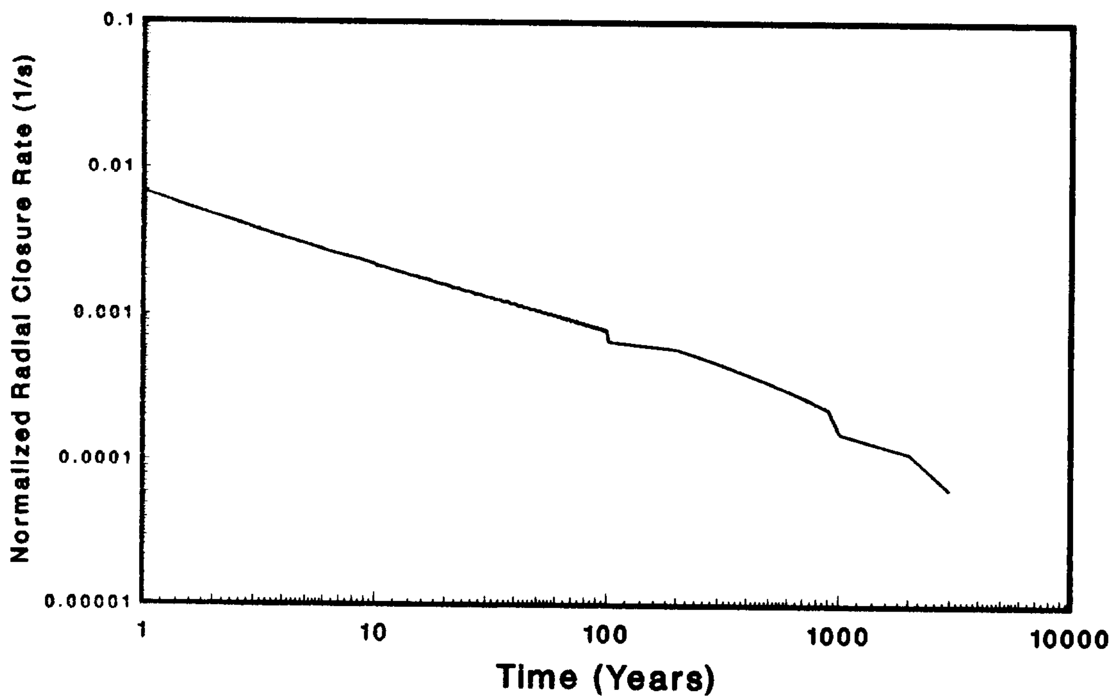

Figure 4.5. Logarithmic Normalized Closure History for Baseline Shaft

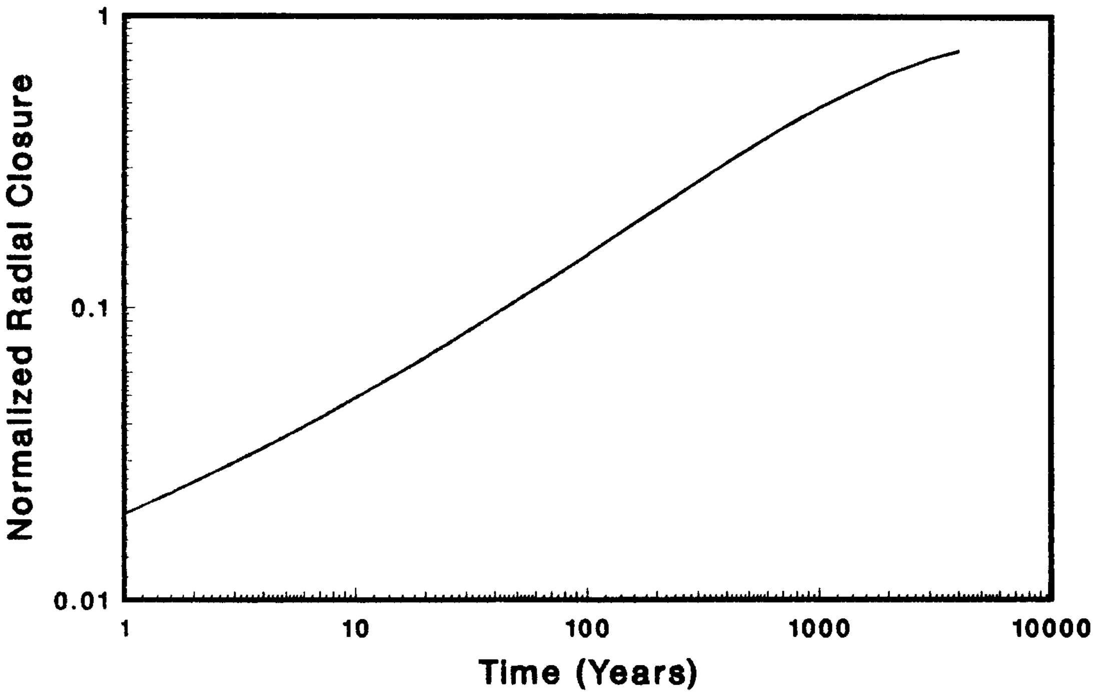

Figure 4.6. Logarithmic Normalized Closure Rate for Baseline Shaft

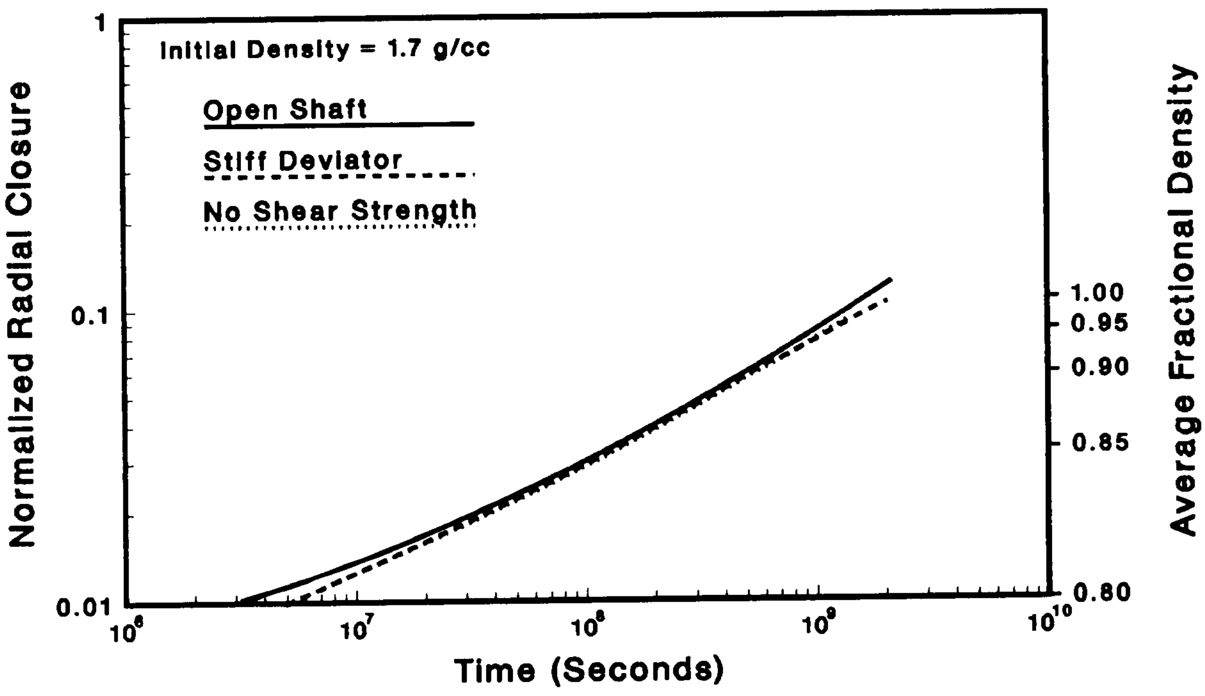

Figure 4.7. Normalized Shaft Closure for Deviatoric Behavior Analyses

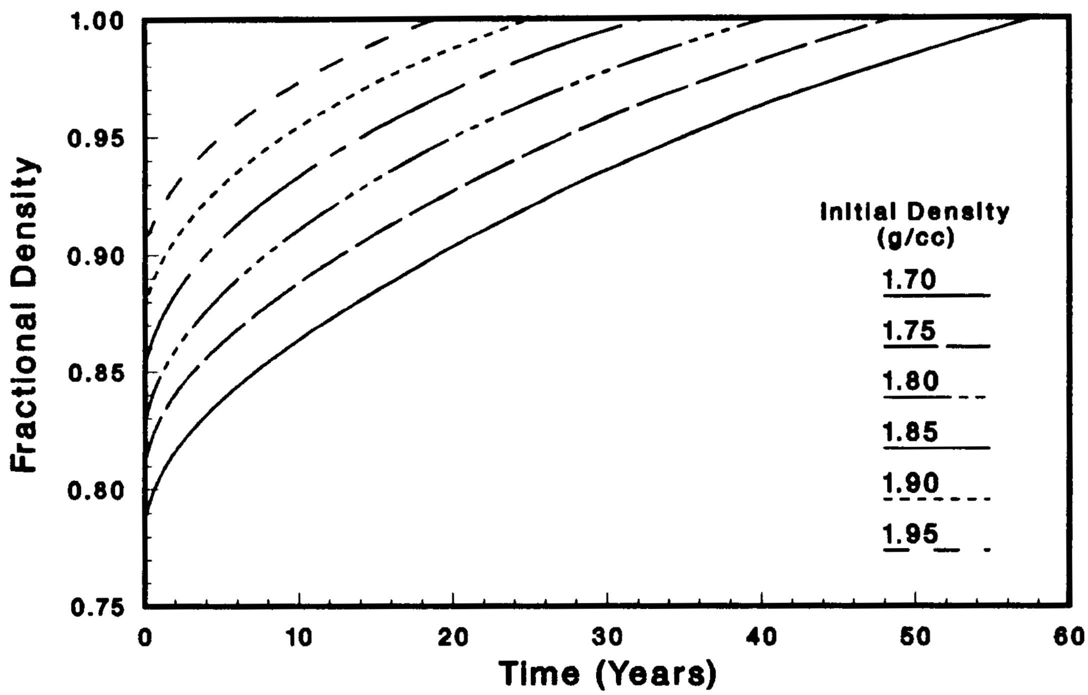

Figure 4.8. Fractional Density vs. Time for Emplacement Density Analyses

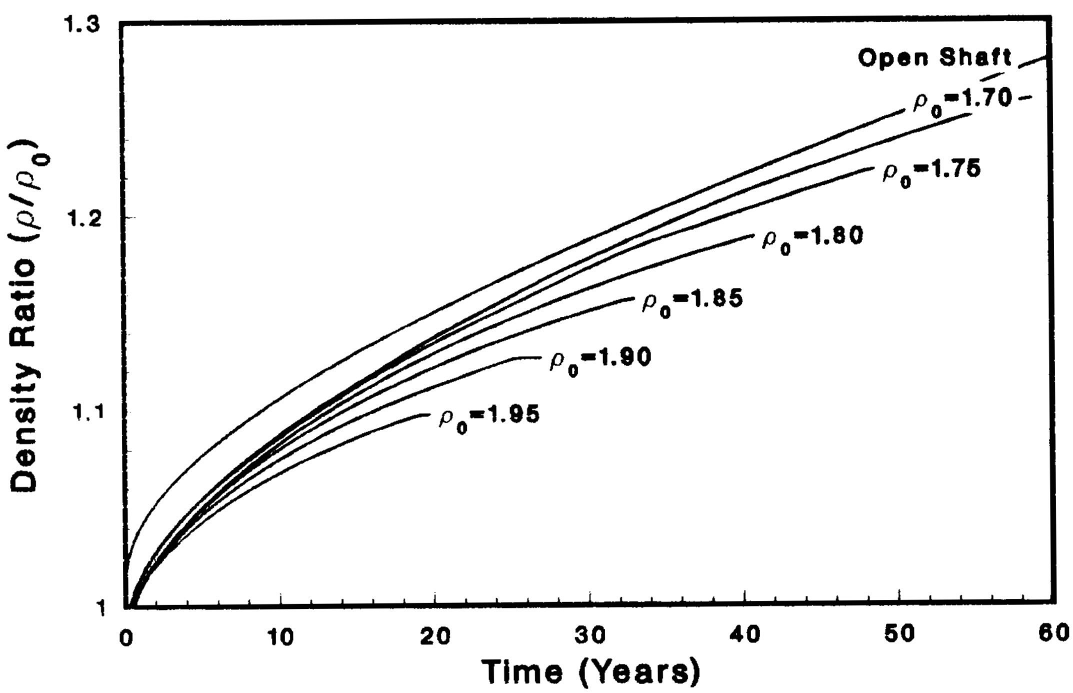

Figure 4.9. Density Ratio vs. Time for Emplacement Density Analyses

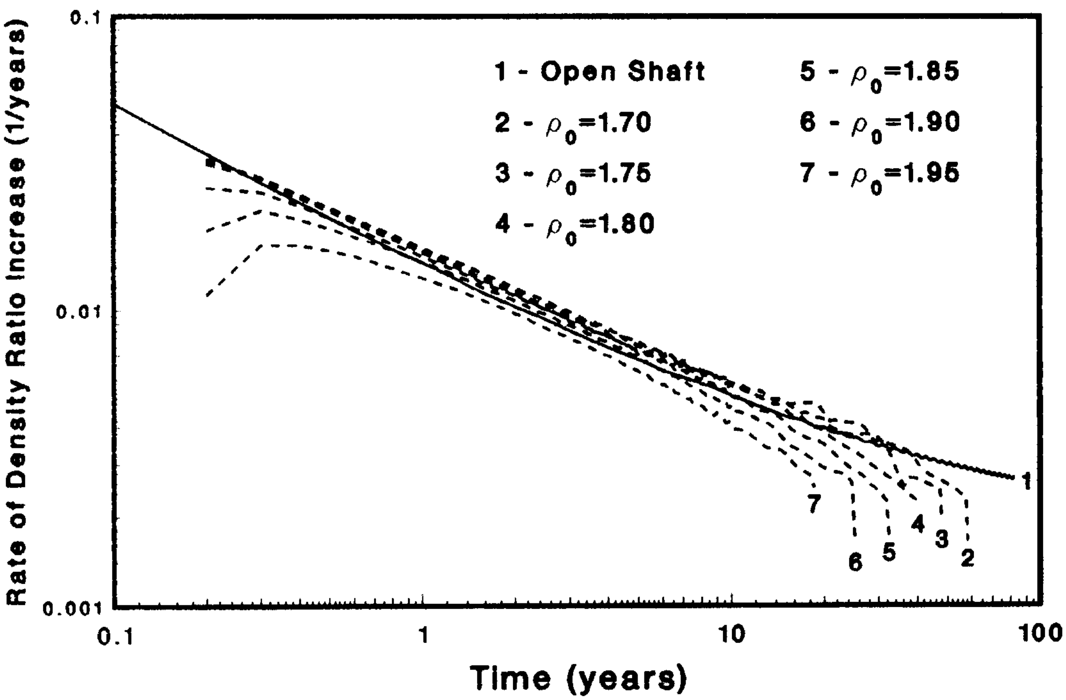

Figure 4.10. Time Rate of Change of Density Ratio for Emplacement Density Analyses

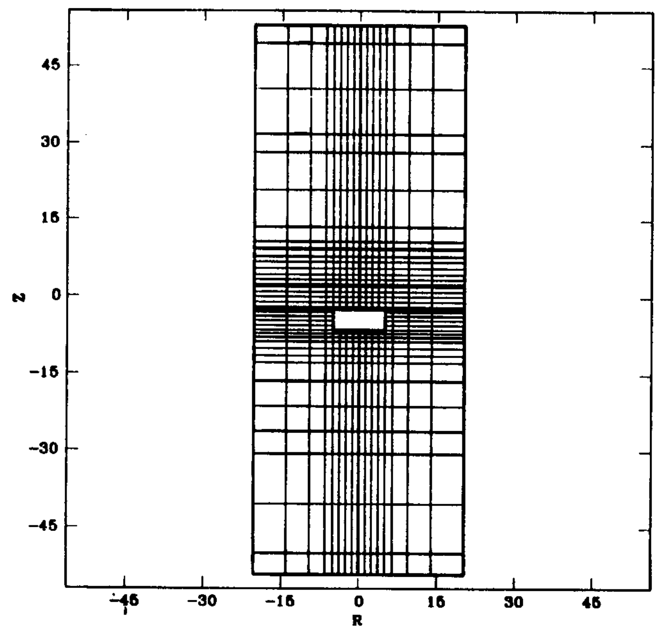

Figure 4.11. Finite Element Mesh for the Crushed Salt, Intact Salt Interaction Analyses—Unbackfilled Drift

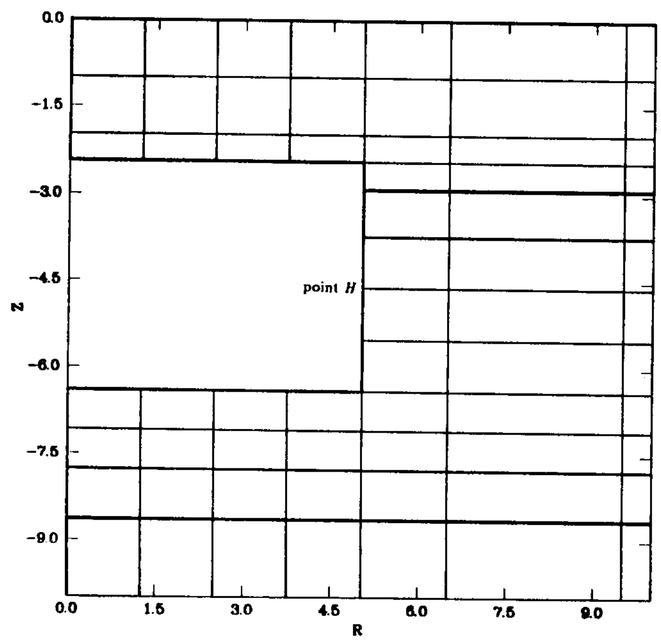

Figure 4.12. Closeup of the Drift Region Mesh for Crushed Salt, Intact Salt Interaction Analyses—Unbackfilled Drift

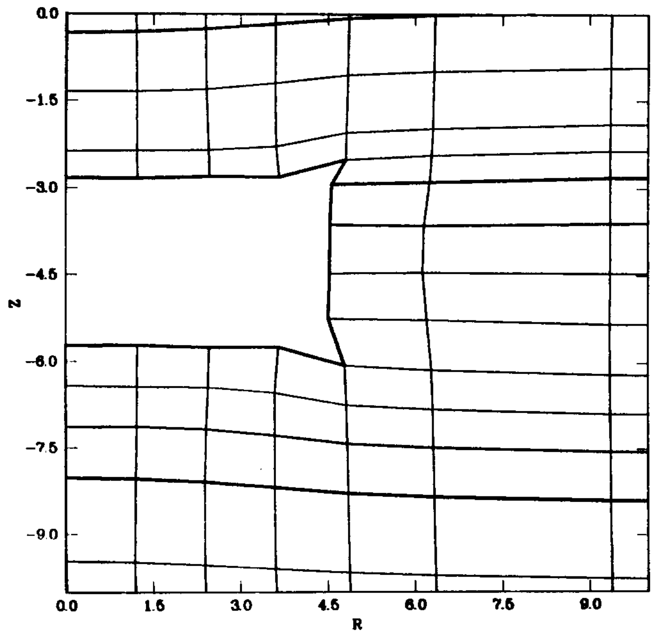

Figure 4.13. Deformed Shape of Square Corner Unbackfilled Drift at 20 Years

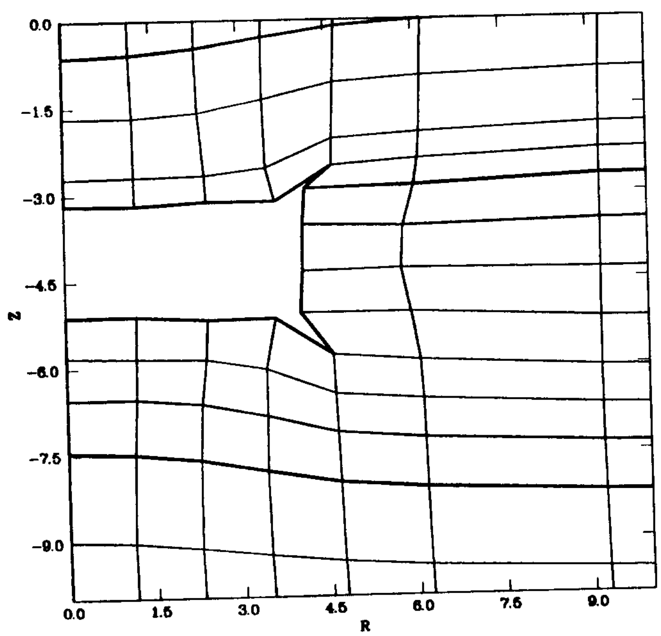

Figure 4.14. Deformed Shape of Square Corner Unbackfilled Drift at 50 Years

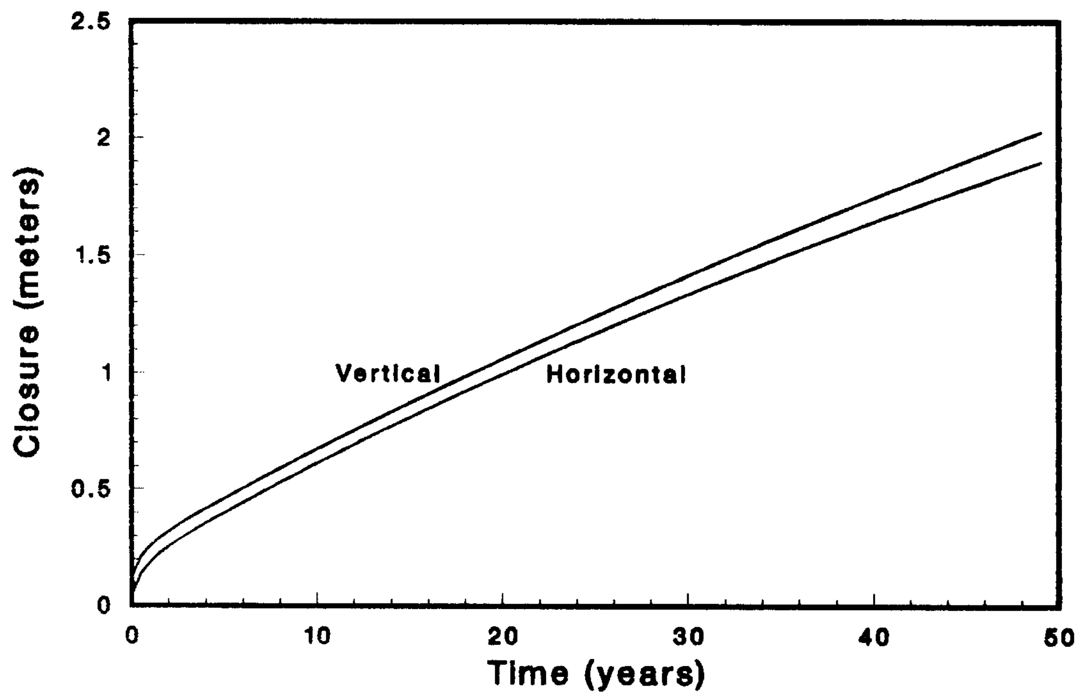

Figure 4.15. Closure Histories for Square Corner Unbackfilled Drift

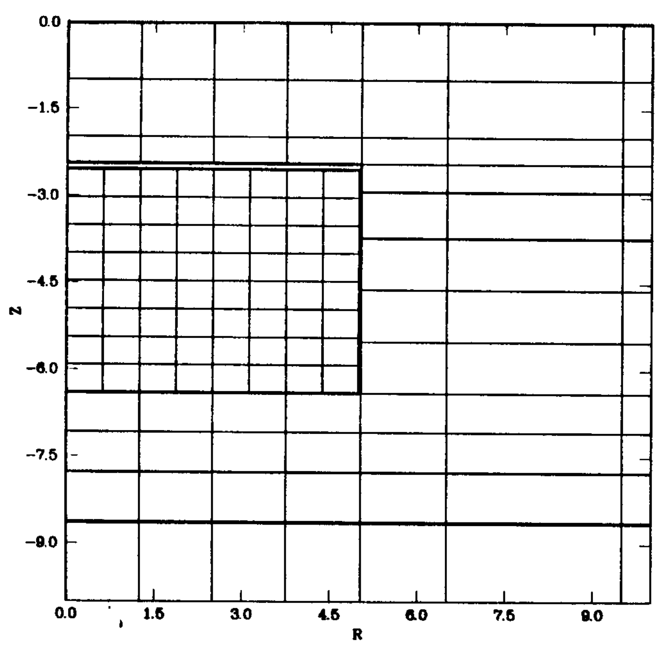

Figure 4.16. Closeup of the Drift Region Mesh for Crushed Salt, Intact Salt Interaction Analyses—Backfilled Drift

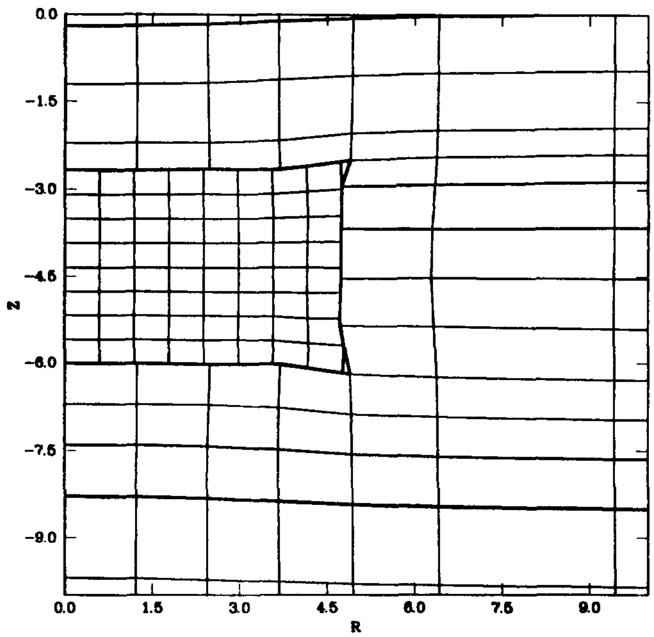

Figure 4.17. Deformed Shape of Square Corner Backfilled Drift at 10 Years

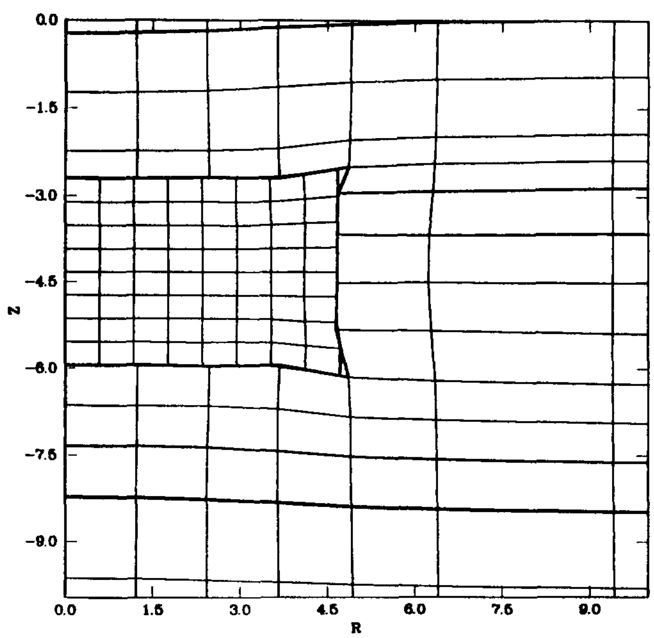

Figure 4.18. Deformed Shape of Square Corner Backfilled Drift at 20 Years

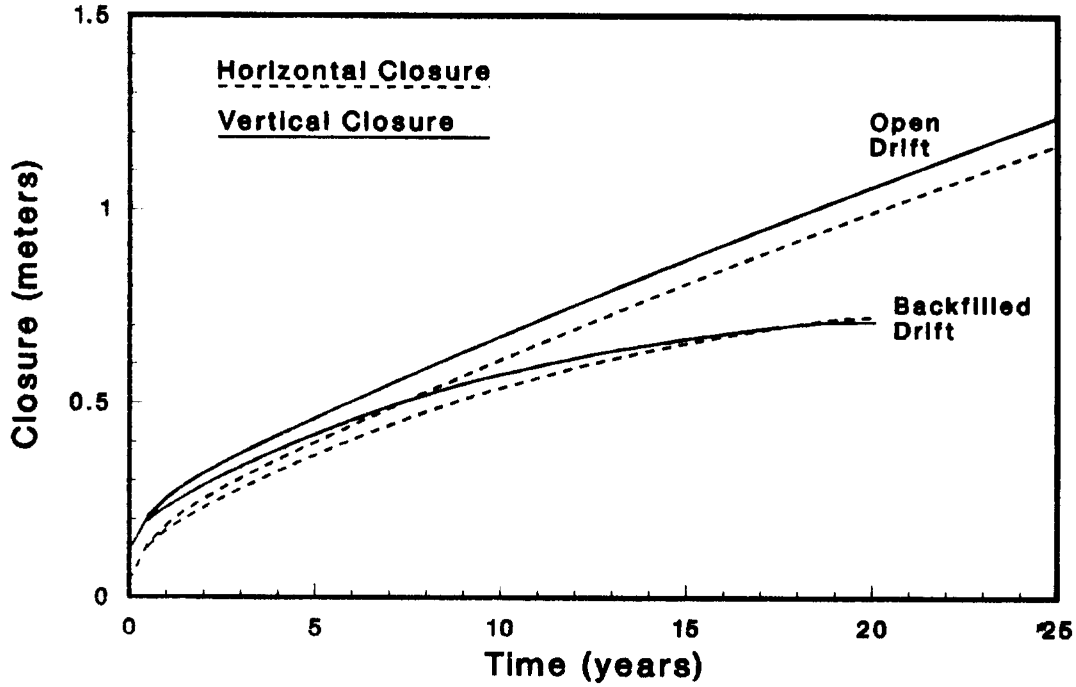

Figure 4.19. Comparison of Closure Histories for Backfilled and Unbackfilled Drift

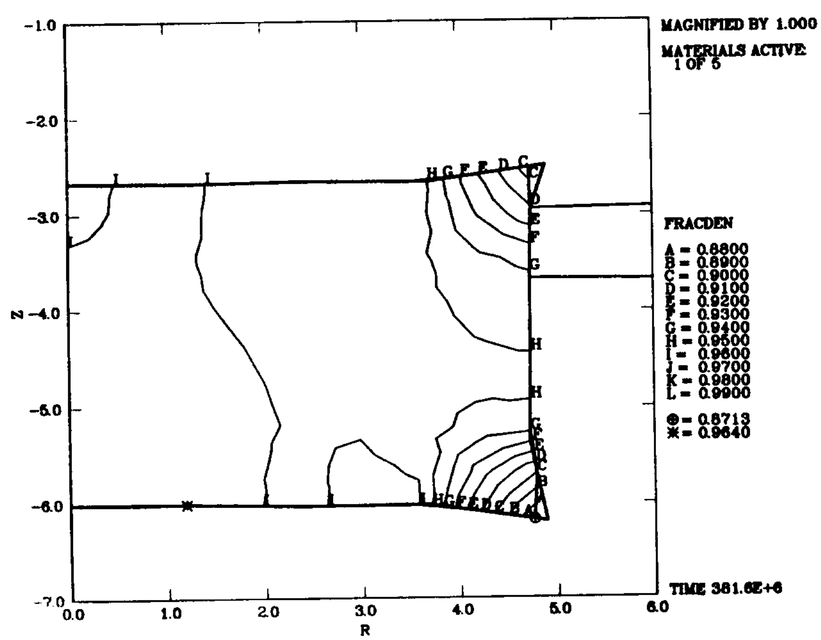

Figure 4.20. Density Contours for Square Corner Backfilled Drift at 10 Years

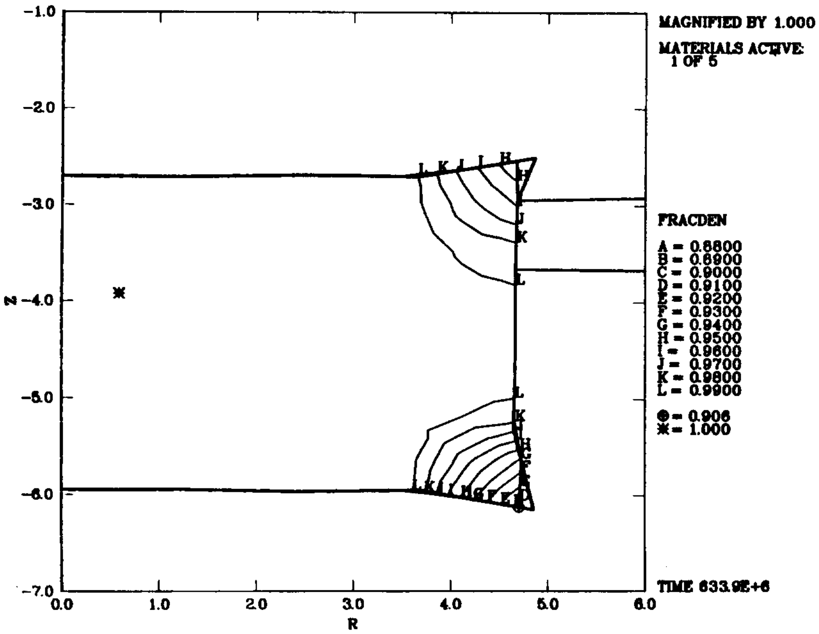

Figure 4.21. Density Contours for Square Corner Backfilled Drift at 20 Years

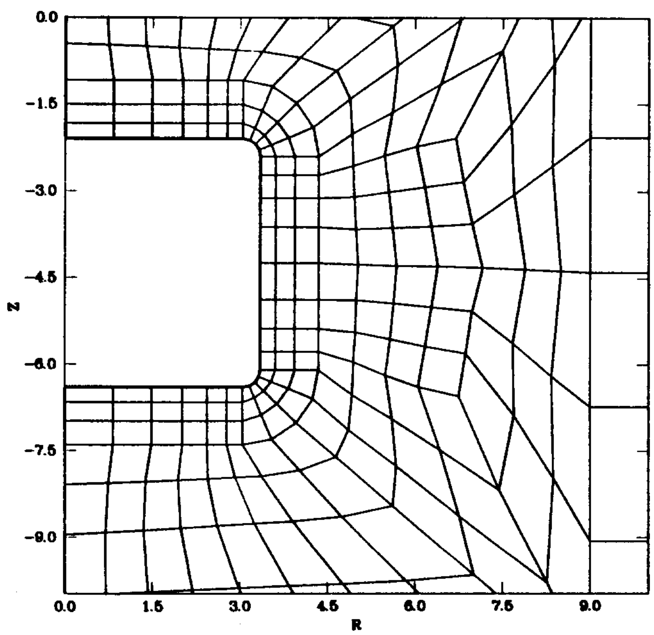

Figure 4.22. Closeup of the Drift Region for the Rounded Corner Drift

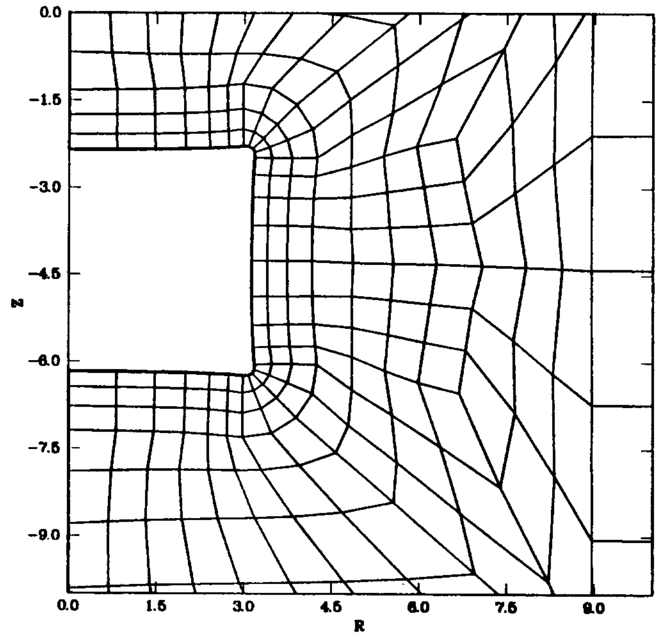

Figure 4.23. Deformed Shape of Rounded Corner Open Drift at 20 Years

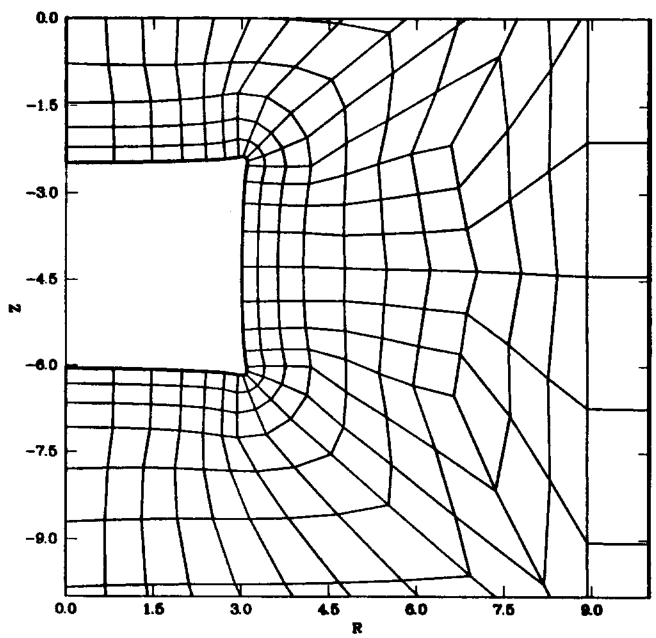

Figure 4.24. Deformed Shape of Rounded Corner Open Drift at 49 Years

5. Summary and Conclusions

The crushed salt constitutive model described in this report represents the current state of the art on the WIPP project in the modeling of crushed salt consolidation. Much research and experimental work remains to be done to more fully develop the model and improve the database upon which it is based. Although it has been shown that the choice of the deviatoric behavior does not significantly affect the volumetric behavior of the crushed salt and the creep behavior of the intact salt, a proper understanding of the deviatoric behavior is necessary to predict effects such as density gradients in the crushed salt. The proper deviatoric response is also necessary to improve the believability of the results predicted by the model. The accuracy of long-term predictions obtained with an *ad hoc* deviatoric model will be very difficult to justify.

More crushed salt consolidation data are needed especially at near intact densities and at lower confining pressures. Experiments are in progress to provide these data and the model will be updated as more data become available. The high density data should provide a more accurate view of the volumetric behavior as the material transitions from a void-dominated creeping material to a creeping solid.

The current model provides the basic capability needed to perform the scoping calculations necessary for support of the WIPP Plugging and Sealing Program. Future work will include:

- Updating the material parameters, and possibly modifying the form of the model, as more experimental data become available.
- Implementing the constitutive model in the two-dimensional, quasistatic, large deformation, inelastic response finite element code SANTOS [21] which is currently under development.
- Generalizing the crushed salt constitutive model and implementing it in the three-dimensional, quasistatic, large deformation, inelastic response finite element code JAC-3D [1] to provide the capability to more accurately analyze the inherently three-dimensional plugging and sealing configurations.
- Performing sensitivity studies to determine the sensitivity of both the model and the response predicted by the model to variations in the material parameters and the configurations analyzed with the model.

- Determining the material parameters to model the consolidation of the crushed salt and bentonite mixture, which is being considered for backfill, when experimental data become available.

References

[1] Biffle, J. H., *JAC—A Two-Dimensional Finite Element Computer Program for the Non-Linear Quasistatic Response of Solids with the Conjugate Gradient Method,* SAND81–0998, Sandia National Laboratories, Albuquerque, NM, 1984.

[2] Gnirk, P. F., "Deformation and Strength Characteristics of Granulated Salt from Laboratory Consolidation Tests," Technical Letter Memorandum, RSI–0020, RE/SPEC Inc., September 25, 1978.

[3] Hansen, F. D., *Experimental Consolidation of Granulated Rock Salt with Application to Sleeve Buckling*, ORNL/Sub-4269/21, prepared for U. S. Department of Energy by Oak Ridge National Laboratory, Oak Ridge, TN, 1976.

[4] Holcomb, D. J. and Shields M. F., *Hydrostatic Consolidation of Crushed Salt with Added Water*, SAND87–1990, Sandia National Laboratories, Albuquerque, NM, 1987.

[5] Holcomb, D. J., "Results of the 55 Day Consolidation Test," internal memo to J. Stormont, 6332, Sandia National Laboratories, Albuquerque, NM, April 19, 1985.

[6] Holcomb, D. J., "Geomechanics Support for WIPP—Monthly Progress Letter, July 1986," internal memo to L. D. Tyler, 6332, Sandia National Laboratories, Albuquerque, NM, August 4, 1986.

[7] Holcomb, D. J., "Geomechanics Support for WIPP—Monthly Progress Letter, February 1987," internal memo to D. Munson and J. Stormont, 6332, Sandia National Laboratories, Albuquerque, NM, February 27, 1987.

[8] Holcomb, D. J., and Hannum, D. W., *Consolidation of Crushed Salt Backfill Under Conditions Appropriate to the WIPP Facility*, SAND82–0630, Sandia National Laboratories, Albuquerque, NM, 1982.

[9] Krieg, R. D., "Implementation of Creep Equations for a Metal Into a Finite Element Computer Program," from *Computer Methods for Nonlinear Solids and Structural Mechanics,* Eds. S. Atluri and N. Perrone, ASME Special Publication AMD Vol. 54, 1983.

[10] Krieg, R. D., *Reference Stratigraphy and Rock Properties for the Waste Isolation Pilot Plant (WIPP) Project*, SAND83–1908, Sandia National Laboratories, Albuquerque, NM, 1984.

[11] McClelland, J. D., "A plastic flow model of hot pressing," *Journal of the American Ceramic Society*, Vol. 44, No. 10, p. 526, 1961.

[12] Morgan, H. S., Krieg, R. D., and Matalucci, R. V., *Comparative Analysis of Nine Structural Codes Used in the Second WIPP Benchmark Problem,* SAND81–1389, Sandia National Laboratories, Albuquerque, NM, 1981.

[13] Morgan, H. S., Stone, C. M., and Krieg, R. D., *An Evaluation of WIPP Structural Modeling Capabilities Based on Comparisons With South Drift Data,* SAND85–0323, Sandia National Laboratories, Albuquerque, NM, 1986.

[14] Pfeifle, T. W. and Senseny, P. E., *Permeability and Consolidation of Crushed Salt From the WIPP Site*, Topical Report RSI–0278, RE/SPEC, Inc., Rapid City, SD, 1985.

[15] *Quarterly Geotechnical Field Data Report, December 1985,* WIPP–DOE–221, U. S. Department of Energy, Waste Isolation Pilot Plant Office, Carlsbad, NM, prepared by Bechtel National, Inc., Advanced Technology Division, San Francisco, CA, 1985.

[16] Ratigan, J. L. and Wagner, R. A., *Thermomechanical Analysis of Crushed-Salt Backfilled Disposal Rooms in a Conceptual Radioactive Waste Repository in Dome Salt*, in Conceptual Design Report, National Waste Terminal Storage Repository for Storing Reprocessing Wastes in a Dome Salt Formation, Special Study No. 2, Vol. XVIII, Stearns-Roger Services, Denver, CO, 1978.

[17] Senseny, P. E., letter to J. C. Stormont dated 16 July, 1986, RSI(RC0)-106/7-86/269, RE/SPEC, Inc., Rapid City, SD.

[18] Sjaardema, G. D. and Krieg, R. D., "Dry Crushed Salt Constitutive Model," unpublished.

[19] Sjaardema, G. D., undocumented computer program.

[20] Stone, C. M., Krieg, R. D., and Beisinger, Z. E., *SANCHO—A Finite Element Computer Program for the Quasistatic, Large Deformation, Inelastic Response of Two-Dimensional Solids*, SAND84–2618, Sandia National Laboratories, Albuquerque, NM, 1985.

[21] Stone, C. M., personal communication, Sandia National Laboratories, Albuquerque, NM, 1987.

[22] Wawersik, W. R., "Geomechanics Support for WIPP—Monthly Progress Letter, December 1985," (Memo to D. E. Munson, 6332, dated January 3, 1986), Sandia National Laboratories, Albuquerque, NM.

[23] Wawersik, W. R. and Hannum, D. W., "Mechanical Behavior of New Mexico Rock Salt in Triaxial Compression Up to 200° C," *Journal of Geophysical Research*, Vol. 85, No. B2, p. 891–900, February 10, 1980.

[24] Zeuch, D. H., Holcomb, D. J., and Lauson, H. S., *Analysis of Consolidation of Granulated Rocksalt Using a Plastic Flow Model for Isostatic Hot-Pressing*, SAND84–1106, Sandia National Laboratories, Albuquerque, NM, 1985.

A. Functional Form of the Elastic Moduli

Table A.1 lists experimentally determined values of the elastic modulus as a function of the density of the crushed salt [8]. These were determined from a test on dry crushed salt in which the hydrostatic pressure was increased to 21 MPa, interrupted by eight depressurization-repressurization cycles. During these unload-reload cycles the response was nearly elastic with little hysteresis. A least squares fit was made to each cycle to determine the bulk modulus of the material at that density.

There are not enough data of this type to define a unique functional form for the bulk modulus; however, another necessary constraint is that the expression must predict the bulk modulus of intact (fully compacted) salt. Thus $K = 20.7$ GPa at a density of 2.14 g/cc [10] must be added to Table A.1. This additional point shows the necessity for a nonlinear function such as an exponential to describe the elastic bulk modulus as a function of the density. The data from Table A.1 together with the additional data point are shown on a semilog plot in Figure A.1. Also shown is a least square fit subject to the constraint that the equation must predict the correct value for intact salt. The equation for the elastic bulk modulus is then

$$K = 17.6\times10^{3}\,e^{6.53\rho} \tag{A.1}$$

where K has units of Pascals and ρ is the density in g/cc. It appears that the fit is acceptable, but without the constraint that the crushed salt have the modulus of intact salt, the trend of the data is somewhat shallower than that predicted by the exponential fit. It is recommended that more tests of this type be made in the future.

Since there have been no experiments to determine the elastic shear modulus, the form of Equation (A.1) is also used to describe the shear modulus. The shear modulus for intact salt is equal to 12.4 GPa [10]. The constraint that the equation correctly predict the intact salt value gives

$$G = 10.6\times10^{3}\,e^{6.53\rho} \tag{A.2}$$

where G has units of Pascals and ρ is the density in g/cc.

Equations (A.1) and (A.2) are also used to describe the elastic moduli of wet crushed salt. No test data are available to support this claim, but it is not expected that the addition of small amounts of water would significantly affect the elastic properties of the material.

Table A.1. Bulk Modulus Data for Dry Crushed Salt Material [8]

Density *(g/cc)*	*Bulk Modulus* *(GPa)*
1.54	0.562
1.62	0.855
1.67	1.269
1.72	1.381
1.76	1.823
1.79	1.557
1.83	1.938
1.87	2.290
1.90	2.700

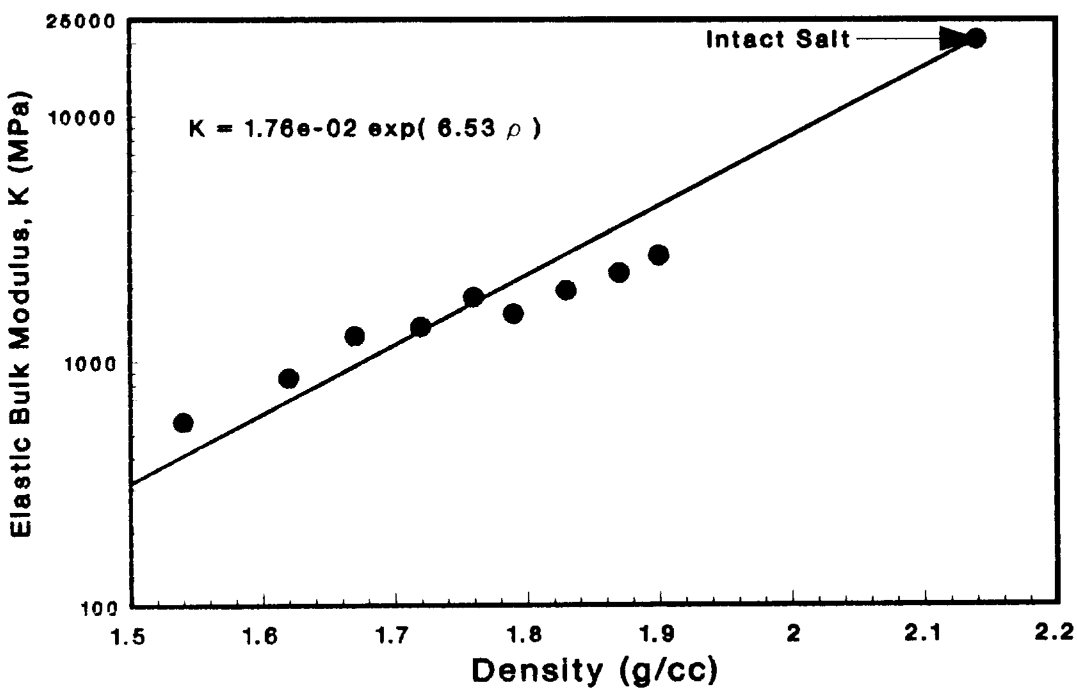

Figure A.1. Bulk Modulus Data for Dry Crushed Salt Material

B. User's Instructions for SANCHO

The crushed salt constitutive model is written as an update deck for SANCHO. The author of this report should be contacted for information concerning the location of this file and for instructions on how to use this model in SANCHO. The constitutive model is currently Material 7 and the information required for the material property specification cards is detailed below in the form used in Reference [20].

MATERIAL TYPE 7 — Crushed Salt Material

MATERIAL, 7, ro, gravx, gravy, omega	CARD 1
MATERIAL TITLE CARD	CARD 2
G_0, G_1, K_0, K_1, A_c, N, Q/R, A, A_1, B_0, B_1, T_0, T_1, Dev, θ	CARD 3

G = Shear Modulus $G = G_0 e^{G_1 \rho}$,
K = Bulk Modulus $K = K_0 e^{K_1 \rho}$,
A_c = Material Constant for deviatoric creep model, see Equation (3.4.6)
N = Stress Power Constant for deviatoric creep model,
Q/R = Exponential Constant for deviatoric creep model,
A = Parameter for Strain Decay, see Equation (2.5.2),
A_1 = 0.0 (Unused),
B = Stress Dependence $B = B_0 e^{B_1 \sigma}$,
T = Yield Stress $T = f(T_0, T_1)$, the values T_0 and T_1 are used in the function relating the yield stress to the density. The form of this function has not yet been determined.
Dev = Deviatoric Model Flag—
0 = Elastic-Plastic Deviatoric Model. If the yield strength is zero, the elastic deviatoric model is used 1 = Elastic-Creep Deviatoric Model
θ = Temperature, currently unused.

The current value of the density is output to the SEACO file as state variable EPX(5); the other 4 variables are unused. A subroutine called INTDEN must be supplied to initialize the density of the crushed salt material. The calling syntax is

```
SUBROUTINE INTDEN (MX,I,EPX)
DIMENSION EPX(*)
```

where MX is the current material number and I is the element number. The array EPX is the state variable array. Elements 5, 10, 15, and 20 of this array must be initialized to the initial crushed salt density.

C. Determination of Crushed Salt Yield Strength

The choice of the proper deviatoric model for crushed salt is very difficult since few data are available. Another problem is the determination of the material parameters to be used in the chosen model. This section describes the method used for the deviatoric model in the backfilled drift analyses. The elastic-plastic deviatoric model was used since the yield strength of the material is the only unknown material parameter. The method described below was used to produce numerically the stiffest possible deviatoric behavior (maximum shear strength).

In the backfilled drift analyses, the yield strength for each element of the backfill and for each time step was chosen such that all of the stress components were compressive or zero if the deviatoric strain rate was compressive. This was done to produce the stiffest backfill material and also to determine numerically the maximum theoretically possible value for the yield stress as a function of the density assuming that the crushed salt can be modeled with an elastic-plastic deviatoric model. The procedure used to produce the stiff backfill model is described below.

For each element and at each time step, trial values of the quantity κ_i^T [see Equation (3.4.4)] for $i = 1, 2, 3$ were calculated for each of the three normal stress components using (no sum on i):

$$\kappa_i^T = \frac{-\sigma_F}{(S_{ii}^0 + 2G\dot{e}'_{ii}t)} \quad \text{if} \quad \dot{e}'_{ii} < 0 \tag{C.1}$$

where t is the load step size, S_{ii}^0 is evaluated at the start and σ_F at the end of the time step. The value of κ used in Equation (3.4.5) was chosen as the minimum of the κ_i^T. The maximum theoretical value of the yield stress at that time step and location was then calculated as

$$\sigma_Y = \sqrt{\tfrac{3}{2}}\,\kappa S^T \tag{C.2}$$

Figure C.1 is a plot showing the variation of the calculated yield stress as a function of the fractional density for the square-cornered backfilled drift calculation. Each point represents the calculated yield stress for an element at a time step during the calculation. The yield stress is seen to vary almost exponentially with the fractional density. A linear regression program [19] was used to find the best fit line relating the natural logarithm of the yield stress to the fractional density. The coefficient of correlation is 0.993 indicating a very good correlation. The t-test for statistical significance indicates that the calculated regression coefficients are significant at the 99.0% confidence level. The least squares best fit equation relating the yield stress to the fractional density is

$$\begin{aligned} \ln \sigma_Y &= -4.10 + 19.21(\rho/\rho_\infty) \\ \sigma_Y &= 1.657 \times 10^{-2} \exp(19.21\rho/\rho_\infty) \end{aligned} \tag{C.3}$$

where σ_Y is the yield stress, ρ is the density, and ρ_∞ is the density of intact salt. This equation is plotted with the data in Figure C.1. Note that this is only a bound on σ_Y, not an actual value; tests will give a value less than this.

Although there are indications of a strong correlation between the yield stress and the fractional density, more research and experimentation are needed to gain a better understanding of the correct deviatoric behavior and the material constants that should be used in the deviatoric model.

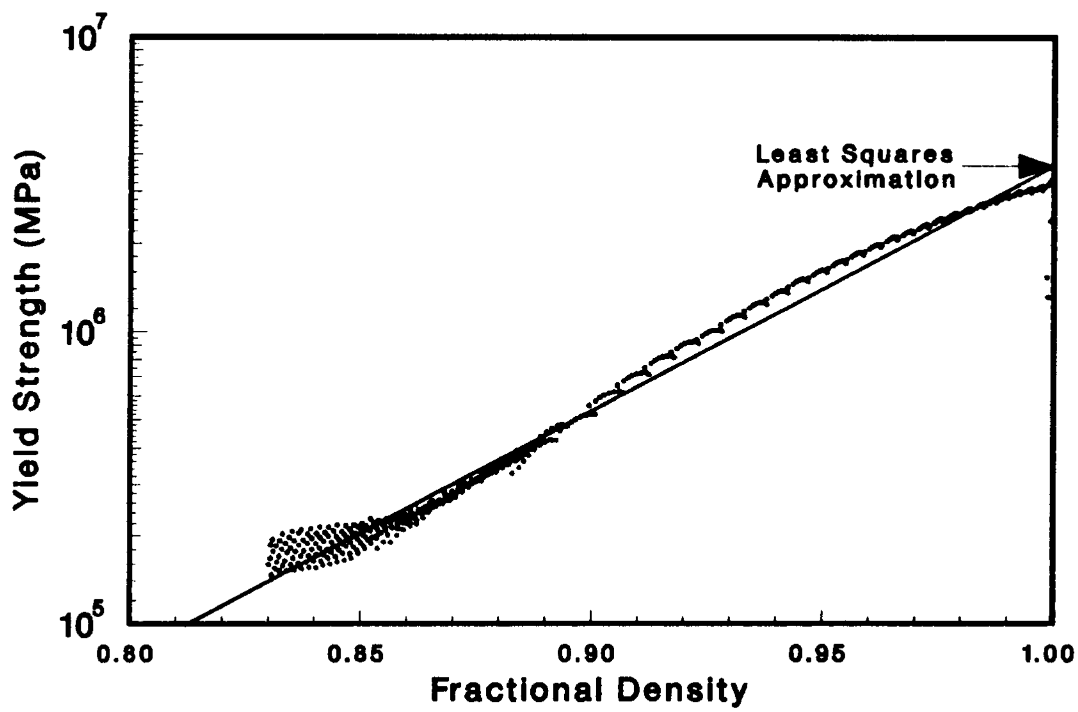

Figure C.1. Variation of Calculated Yield Stress with Fractional Density

Distribution:

U. S. Department of Energy, (5)
Office of Civilian Radioactive Waste
Management
Office of Geologic Repositories
Forrestal Building
Washington, DC 20585
Stephen H. Kale - RW-20
Associate Director
T. H. Isaacs - RW-20
Deputy Associate Director
James C. Bresee - RW-22
Director, Repository Coordination Div.
Ralph Stein - RW-23
Director, Engineering & Geotechnology
James P. Knight - RW-24
Director, Siting, Licensing and Quality
Assurance

U.S. Department of Energy (3)
Albuquerque Operations
P.O. Box 5400
Albuquerque, NM 87185
G. C. Romatowski
J. E. Bickel
D. G. Jackson, Director, Public Affairs
Division

U.S. Department of Energy (8)
WIPP Project Office (Carlsbad)
P.O. Box 3090
Carlsbad, NM 88221
J. Tillman (4)
A. Hunt
T. Lukow (2)
R. Eastmond

U. S. Department of Energy, SRPO (4)
Salt Repository Project Office
505 King Avenue
Columbus, OH 43201
J. O. Neff
R. Wunderlich
G. Appel
R. Wu

U. S. Department of Energy
Research & Technical Support Division
P.O. Box E
Oak Ridge, TN 37830
D. E. Large

U. S. Department of Energy
Richland Operations Office
Nuclear Fuel Cycle & Production Division
P.O. Box 500
Richland, WA 99352
R. E. Gerton

U. S. Department of Energy (4)
Office of Defense Waste and Transportation
Management
Washington, DC 20545
J. E. Dieckhoner — DP-122
L. H. Harmon — DP-121
A. Follett — DP-121
J. Mather — DP-121

U. S. Department of Energy (2)
Idaho Operations Office
Fuel Processing and Waste Management
Division
785 DOE Place
Idaho Falls, ID 83402

U. S. Department of Energy (4)
Savannah River Operations Office
Waste Management Project Office
P.O. Box A
Aiken, SC 29801
S. Cowan
W. J. Brumley
J. R. Covell
D. Fulmer

U. S. Department of the Interior
959 National Center
Geological Survey
Reston, VA 22092
E. Roedder

Distribution (continued):

U.S. Nuclear Regulatory Commission (4)
Division of Waste Management
Mail Stop 623SS
Washington, D.C. 20555
Michael Bell
Hubart Miller
Jacob Philip
NRC Library

F. R. Cook
Nuclear Regulatory Commision
HLW Licensing Branch, Materials Section
MS 905 SS
Washington, DC 20555

U. S. Geological Survey
Special Projects
MS954, Box 25046
Denver Federal Center
Denver, CO 80255
R. Snyder

U. S. Geological Survey
Conservation Division
P.O. Box 1857
Roswell, NM 88201
W. Melton

U. S. Geological Survey
Water Resources Division
Western Bank Bldg.
505 Marquette, NW, #720
Albuquerque, NM 87102
H. Lee Case
Peter Davies

State of New Mexico (2)
Environmental Evaluation Group
320 Marcy Street
P.O. Box 968
Santa Fe, NM 87503
Robert H. Neill, Director

NM Department of Energy & Minerals (2)
P.O. Box 2770
Santa Fe, NM 87501
Kasey LaPlante, Librarian

New Mexico Bureau of Mines and Mineral Resources (2)
Socorro, NM 87801
F. E. Kottolowski, Director
J. Hawley

Battelle Pacific Northwest Laboratories (6)
Battelle Boulevard
Richland, WA 99352
D. J. Bradley
J. Relyea
R. E. Westerman
S. Bates
H. C. Burkholder
L. Pederson

Bureau of Land Management
Branch of Solid Minerals
NM–921, Box 1449
Santa Fe, NM 87503
James Olsen

Battelle Memorial Institute (16)
Project Management Division
505 King Avenue
Columbus, OH 43201
ONWI Library
W. Carbiener, General Manager (3)
S. Basham
P. Hoffman
H. R. Hume
H. N. Kalia
J. Kircher
D. Moak
J. Moody
L. Page
G. Raines
J. Schornhorst
O. Swanson
J. Treadwell

Distribution (continued):

Bechtel, Inc. (5)
P.O. Box 3965
45-11-B34
San Francisco, CA 94119
E. Weber
M. Beathard
H. Taylor
P. Frobenius
D. L. Wu

INTERA Technologies, Inc. (2)
6850 Austin Center Blvd., #300
Austin, TX 78731
G. E. Grisak
J. F. Pickens

INTERA Technologies, Inc.
P.O. Box 2123
Carlsbad, NM 88221
Wayne Stensrud

IT Corporation (2)
P.O. Box 2078
Carlsbad, NM 88221
W. Patrick
R. McKinney

IT Corporation (2)
2340 Alomo, SE
Suite 306
Albuquerque, NM 87106
W. R. Coons
P. Kelsall

RE/SPEC Inc. (7)
P.O. Box 725
Rapid City, SD 57701
P. F. Gnirk
L. L. Van Sambeek
D. B. Blankenship
T. Brandshang
G. Callahan
T. Pfeifle
J. L. Ratigan

RE/SPEC Inc.
P.O. Box 14984
Albuquerque, NM 87191
S. W. Key

E. I. Dupont de Nemours Company (6)
Savannah River Laboratory
Aiken, SC 29801
N. Bibler
E. L. Albenisius
M. J. Plodinec
G. G. Wicks
C. Jantzen
J. A. Stone

E. I. Dupont de Nemours Company
Savannah River Plant
Aiken, SC 29801
R. Baxter

George Dymmel
SAIC
101 Convention Center Dr.
Las Vegas, NV 89109

Systems, Science, and Software (2)
Box 1620
La Jolla, CA 92038
E. Peterson
P. Lagus

University of Arizona
Department of Nuclear Engineering
Tucson, AZ 85721
J. G. McCray

University of Arizona
Department of Mining and Gelogical
Engineering
Tucson, AZ 85721
J. J. K. Daemen

Distribution (continued):

University of New Mexico (2)
Geology Department
Albuquerque, NM 87131
D. G. Brookins
Library

The Pennsylvania State University (3)
Materials Research Laboratory
University Park, PA 16802
Della Roy
Rustrum Roy
Will White

Texas A&M University
Center of Tectonophysics
College Station, TX 77840
John Handin

University of Texas at El Paso
Department of Geological Sciences
El Paso, TX 79968
D. W. Powers

Westinghouse Electric Corporation (9)
P.O. Box 2078
Carlsbad, NM 88221
Library
R. Mairson
V. DeJong
W. Chiquelin
T. Dillon
V. Likar
J. Johnson
J. Sadler
R. Kehrman

National Academy of Sciences, (8)
WIPP Panel

Dr. B. Krauskopf, Chairman
Department of Geology
Stanford University
Stanford, CA 94305

Frank L. Parker, Vice Chairman
Department of Environmental and
Water Resources Engineering
Vanderbilt University
Nashville, TN 37235

John O. Blomeke
Oak Ridge National Laboratory
P.O. Box X
Oak Ridge, TN 37830

John D. Bredehoeft
Western Region Hydrologist
Water Resources Division
U. S. Geological Survey
345 Middlefield Road
Menlo Park, CA 94025

Dr. Karl P. Cohen, Member
928 N. California Avenue
Palo Alto, CA 94303

Fred M. Ernsberger, Member
1325 N.W. 10^{th} Avenue
Gainesville, FL 32611

Hans P. Eugster
Johns Hopkins University
Department of Earth Sciences
Baltimore, MD 21218

Rodney C. Ewing
University of New Mexico
Department of Geology
Albuquerque, NM 87131

Charles Fairhurst
University of Minnesota
Department of Geological Sciences
Minneapolis, MN 55455

William R. Muehlberger
University of Texas at Austin
Department of Geological Sciences
Austin, TX 78712

Distribution (continued):

D'Arcy A. Shock, Member
233 Virginia
Ponca City, OK 74601

National Academy of Sciences (2)
Committee on Radioactive Waste
Management
2101 Constitution Avenue, NW
Washington, D.C. 20418
Peter Meyers
Remi Langum

Hobbs Public Library
509 N. Ship Street
Hobbs, NM 88248
Ms. Marcia Lewis, Librarian

New Mexico Tech
Martin Speere Memorial Library
Campus Street
Socorro, NM 87810

New Mexico State Library
P.O. Box 1629
Santa Fe, NM 87503
Ms. Ingrid Vollenhofer

Zimmerman Library
University of New Mexico
Albuquerque, NM 87131
Zanier Vivian

WIPP Public Reading Room
Atomic Museum, Kirtland East AFB
Albuquerque, NM 87185
Ms. Gwynn Schreiner

WIPP Public Reading Room
Carlsbad Municipal Library
101 S. Halagueno Street
Carlsbad, NM 88220
Lee Hubbard, Head Librarian

Thomas Brannigan Library
106 W. Hadley Street
Las Cruces, NM 88001
Don Dresp, Head Librarian

Roswell Public Library
301 N. Pennsylvania Avenue
Roswell, NM 88201
Ms. Nancy Langston

Svensk Karnbransleforsorjning AB
Project KBS
Karnbranslesakerhet
Box 5864
10248 Stockholm, SWEDEN
Fred Karlsson

Institut für Tieflagerung (4)
Theodor-Heuss-Straße 4
D-3300 Braunschweig
FEDERAL REPUBLIC OF GERMANY
K. Kuhn
H. Gies
N. Jockwer
H. Gies

Bundesanstalt für Geowissenschaften und
Rohstoffe (3)
Postfach 510 153
3000 Hannover 51
FEDERAL REPUBLIC OF GERMANY
M. Langer
M. Wallner
U. Hunsche

Hahn-Meitner-Institut für Kernforschung
Glienicker Straße 100
1000 Berlin 39
FEDERAL REPUBLIC OF GERMANY
Werner Lutze
Klaus Eckart Maass

Distribution (continued):

Bundesministerium für Forschung und
Technologie
Postfach 200 706
5300 Bonn 2
FEDERAL REPUBLIC OF GERMANY
Rolf-Peter Randl

Physikalisch-Technische Bundesanstalt (2)
Bundesanstalt 100, 3300 Braunschweig
FEDERAL REPUBLIC OF GERMANY
Helmut Rothemeyer
Peter Brenneke

Kernforschug Karlsruhe (3)
Postfach 3640
7500 Karlsruhe
FEDERAL REPUBLIC OF GERMANY
R. Koster
Reinhard Kraemer
K. D. Closs

Studiecentrum Voor Kernenergie (2)
Centre D'Energie Nucleaire
SCK/CEN
Boeretang 200
b–2400 Mol
BELGIUM
Mr. A. Bonne
Pierre Van Iseghem

Atomic Energy of Canada, Ltd. (2)
Whiteshell Research Estab.
Pinewa, Manitoba, CANADA
ROE 1L0
Peter Haywood
John Tait

Dr. D. K. Mukerjee
Ontario Hydro Research Lab
800 Kipling Avenue
Toronto, Ontario, CANADA
MBZ 554

Claude Sombret
Centre D'Etudes Nucleaires
De La Vallee Rhone
CEN/VALRHO
S.D.H.A. BP 171
30205 Bagnols-Sur-Ceze
FRANCE

Mr. Jean-Pierre Olivier
OECD Nuclear Energy Agency
Division of Radiation Protection and Waste
Management
38, Boulevard Suchet
75016 Paris, FRANCE

D. R. Knowles
British Nuclear Fuels, plc
Risley, Warrington, Cheshire WA3 6AS
1002607 GREAT BRITAIN

Shingo Tashiro
Japan Atomic Energy Research Institute
Tokai-Mura, Ibaraki-Ken
319–11 JAPAN

Netherlands Energy Research Foundation
ECN (2)
3 Westerduinweg
P.O. Box 1
1755 ZG Petten, THE NETHERLANDS
Tuen Deboer, Mgr.
L. H. Vons

Dr. R. O. Pohl
Cornell University
Department of Physics
Clark Hall
Ithaca, NY 14853

Pannell Library
New Mexico Junior College
Lovington Highway
Hobbs, NM 88240
Ms. Ruth Hill

Distribution (continued):

George Pinder
Princeton University
Department of Civil Engineering
Princeton, NJ 08540

Argonne National Laboratory (5)
9700 South Cass Avenue
Argonne, IL 60439
A. M. Friedman
D. Hambeley
W. Harrison
N. Meldgin
M. Steindler

Los Alamos Scientific Laboratory
Los Alamos, NM 87545
B. Erdal, CNC–11

Oak Ridge National Laboratory (4)
Box Y
Oak Ridge, TN 37830
R. E. Blanko
E. Bondietti
C. Claiborne
G. H. Jenks

Oak Ridge National Laboratory, Bldg. 2001
Ecological Sciences Information Center
P.O. Box X
Oak Ridge, TN 37830
C. S. Fore

Rockwell International (2)
Rocky Flats Plant
Golden, CO 80401
W. S. Bennett
C. E. Wickland

Rockwell International (3)
Atomics International Division
Rockwell Hanford Operations
P.O. Box 800
Richland, WA 99352
J. Nelson (HWVP)
P. Salter
W. W. Schultz

U. S. Army Corps of Engineers
Waterways Experiment Station
P.O. Box 631
Vicksburg, MS 30180

C. H. Conley
School of Civil and Environmental Engineering
Hollister Hall
Cornell University
Ithaca, NY 14853

Sandia Internal:

1510 J. W. Nunziato
1520 C. W. Peterson
1521 R. D. Krieg (15)
1521 D. S. Preece
1521 H. S. Morgan
1521 D. J. Segalman
1521 C. M. Stone
1521 G. D. Sjaardema (15)
1530 L. W. Davison
1550 R. C. Maydew
1832 W. B. Jones
1832 J. W. Munford
1832 J. A. Van Den Dyke
1833 G. A. Knorovsky
1840 R. J. Eagan
1841 R. B. Diegle
1841 N. R. Sorensen
2122 F. G. Yost
3141-1 S. A. Landenberger (5)
3151 W. L. Garner, (3)
For: DOE/TIC (Unlimited Release)
3154-3 C. H. Dalin, (28)
For: DOE/TIC
6000 D. L. Hartley
6232 W. R. Wawersik
6232 D. J. Holcomb
6232 D. H. Zeuch
6300 R. W. Lynch
6310 T. O. Hunter
6330 W. D. Weart
6331 A. R. Lappin

Distribution (continued):

6331 D. J. Borns
6331 C. L. Stein
6332 L. D. Tyler
6332 J. G. Argüello
6332 R. Beraun
6332 R. V. Matalucci
6332 D. E. Munson
6332 E. J. Nowak (5)
6332 J. C. Stormont
6332 T. M. Torres
6332 Sandia WIPP Central Files (2) (HLW)
6334 D. R. Anderson
7100 C. D. Broyles
7110 J. D. Plimpton
7116 S. R. Dolce
7116 C. W. Cook
7120 M. J. Navratil
7125 R. L. Rutter
7125 J. T. McIlmoyle
7130 J. O. Kennedy
7133 R. D. Statler
7133 J. W. Mercer
7133 H. C. Walling
7135 P. D. Seward
8024 P. W. Dean
8310 R. W. Rhode
8314 S. L. Robinson
8314 N. R. Moody
8314 M. W. Perra
8315 L. A. West